Application of Digital Imaging Correlation to Brain Deformation

Thesis

Presented in Fulfillment of the Requirements for an Undergraduate Honors Thesis in Biomedical Engineering

By

Vincent Schreck

The Ohio State University

2019

Thesis Committee

Advisor: Yun Seok Kang, PhD

Committee Member: John H. Bolte IV, PhD

Contents

Abstract

Shear deformation and strain are important to be quantified to evaluate computational models of the brain; however, it is challenging to get measurements at the meningeal layer. Strain gauges can be attached to hard tissues, such as bone, but cannot be attached to soft tissue, such as the brain. This study proposes using Digital Imaging Correlation (DIC) to analyze high-speed, high-frequency, B-mode ultrasound images to track the displacement and strain of a postmortem human subject (PMHS) brain tissue during anterior/poster motions that would be likely to cause a subdural hematoma. DIC makes it possible to calculate strain and displacement by looking at how points move across a series of images taken over time. Current commercial point-tracking software, such as TEMA which is used in Injury Biomechanics, typically only tracks points rather than performing a strain analysis. The head was placed in a device that generated rotational motion. The PMHS head was tested under high, medium, and low severities. A subset size of 20, a subset spacing of 3, and a strain radius of 3 were used to analyze the medium severity ultrasound images with DIC. The DIC parameters were supported by a parametric study that used images of a metal sample in tension. Both displacement plots and strain plots were created from the analysis. The maximum x displacement measurements at different depths were validated with TEMA. The percent difference of the displacement measurements between the two methods was 2.22% at 1 mm deep and 2.24% at 2 mm deep into the brain tissue. At the surface of the brain tissue, the percent difference was 32%. The strain plots were less conclusive due to a large quantity of noise. It was concluded that DIC can accurately measure displacement but not strain from ultrasound images of the brain.

List of Figures

List of Tables

Chapter 1: Introduction

Acute subdural hematomas (ASDHs) are a growing concern among people age 54 and older. Subdural hematomas are when blood pools beneath the dura mater, one of the meninges, applying pressure on the brain. Subdural hematomas are especially a concern in elderly victims of motor vehicle crashes (MVCs). Elderly victims are more likely to develop a subdural hematoma, and the mortality rate is as high as 50% for those who do develop a subdural hematoma. The number of patients age 65 or older with an ASDH is projected to be 135% greater than the corresponding value from the year 2000. From this prior research, it was determined that more research needed to be done to study the relationship between brain deformation and subdural hematomas. Specifically, the relationship between brain deformation and ASDHs caused by the failure of the bridging veins from anterior/posterior head impacts was of interest for this new study. The bridging veins run along the surface of the brain tissue and toward the dura mater; therefore, shear deformation between the brain tissue and the dura mater can cause a rupture of the bridging vein. Blood can then pool beneath the dura to cause a subdural hematoma (Mallory, 2010). The shear deformation and strain are important to be quantified to evaluate computational models of the brain and to predict which severities of head motions cause injury to brain tissue. Current methods of analyzing brain motion by the meningeal layer have been challenging. A new method is being proposed that would involve analyzing high-speed, high-frequency, B-mode ultrasound images to quantify brain deformation and motion near the meningeal layer.

Digital Imaging Correlation (DIC) is a method of tracking points across subsequent images taken of an object. This makes it possible to study displacement and strain properties of an object of interest (Pan, 2009). The specific algorithm being analyzed in this study computes a two-dimensional (2D) DIC and has significant potential in the field of Injury Biomechanics. Traditional measurements of strain require a complex setup of multiple strain gauges. In contrast, DIC requires no significant setup for the analysis. It is also important to note that the usefulness of strain gauges is limited by where they can physically be placed. For example, strain gauges are unable to be placed on soft tissues, such as brain tissue; however, strain gauges can be placed on harder tissues, such as bone. Point-tracking commercial software, such as TEMA which is commonly used in Injury Biomechanics, only directly measures displacement. Strain measurements in 2D are not calculated directly by current software on the market. Any measurements of strain must be calculated by the researcher which introduces a potential source of error. Additionally, TEMA can only track individual points while DIC can generate vector fields that display both displacement and strain over a region in 2D. Therefore, DIC has an advantage over TEMA in that it can analyze a large quantity of points at once. Because DIC analyzes images, it can theoretically be used to analyze images taken from current medical imaging techniques. The hypothesis for this study was that DIC would be a better way of accurately measuring both the displacement and strain from ultrasound images of brain tissue from anterior/posterior head motions compared to TEMA and other commercial point-tracking software.

The purpose of this study was to explore using DIC as a method of analyzing the displacement and strain of the brain tissue of postmortem human subject (PMHS) heads in anterior/posterior motions that could cause subdural hematomas. The motion of the PMHS brain tissue was recorded with ultrasound imaging. The strain measurements of the brain are especially important for investigating subdural hematomas and evaluating computational brain models. This is primarily because biological samples do not act as rigid bodies but rather display complex viscoelastic properties. During deformation, a mixture of compression, tension and shear occurs which then leads to patterns of strain within the tissue. Due to the viscoelastic properties of brain tissue, the deformation is also highly dependent on the shear rate. Brain injuries can occur when the strain exceeds 10% and the strain rate

exceeds 10/s (Rashid et al, 2013). The strain properties of brain tissue are difficult to measure and not well reported; therefore, an innovation in the way of measuring strain of brain tissue could be a significant step forward in the field of Injury Biomechanics. Another point to consider is that the importance of strain can vary at different severities of anterior/poster head motion. As the severity of the head motion increases, the importance of strain to brain deformation also increases. Therefore, this study also analyzed brain deformation at different severities of anterior/posterior head motions (Hardy et al, 2007).

The DIC method is thought to have a lot of potential as it has been successfully used on other applications in the past. However, no prior analysis exists for using DIC to analyze PMHS brain motions. One specific DIC application used the technique to study images of a steel-concrete connection. Using DIC, the bond-slip relationship at the surfaces of the two materials was analyzed. Strain gauges were used as a control to which the DIC data could be compared. Both methods were shown to have a similar trend in the data (Biscaia et al. 2018). With a more complicated setups, 3D DIC analyses have also been performed. One application of this technique involved looking at the deformation of multiple layers in complex electrical devices (Niu et al. 2018). Most of the tests done so far with DIC analysis have been done with a static load; however, some progress has been made in performing a DIC analysis under a dynamic load. This was able to be done by using a lock-in amplifier. (Chen et al. 2018). Progress also has been made in using DIC analysis with only two images as opposed to a series of images. Experiments for this were performed by using software to estimate what the intermediate images were. These intermediate images could then be used in the DIC analysis (Genovese et al. 2018).

This study was split into two phases. First, a parametric study was performed on a set of sample images to determine the optimum parameters for the DIC analysis of the ultrasound brain images. The sample images consisted of a metal sample with a hole in the center undergoing a tensile test. Because the sample was not viscoelastic, it was easier to analyze the results of the analyses. The second phase of the study involved analyzing the ultrasound images with DIC with the optimum parameters that were determined from the first part of the study. The two phases of this study made it possible to learn more about the parameters involved in a DIC analysis and to see if DIC can produce valid results for displacement and strain measurements of brain tissue. If this goal were achieved, it could lead to better testing methods to avoid scenarios that could cause a subdural hematoma or other brain deformation-related injuries.

Chapter 2: Methodology

2.1 Image Collection

To study shear motion of the brain relative to the dura mater, five major components were used: a high-speed, high-frequency, B-mode ultrasound machine (abbreviated as B-mode ultrasound) with a corresponding ultrasound probe, a rotational fixture, post-mortem human subject (PMHS) heads, angular rate sensors (ARSs), accelerometers, and a pressure sensor. The PMHS were not excluded based on age or gender. The rotational fixture setup was used to model the anterior/posterior head movements that are possible to cause a subdural hematoma. Three different sets consisting of an angular velocity and an angular acceleration were used. These three different sets represented low-severity, medium-severity, and high-severity cases. The testing parameters are shown in Table 1 located below. The medium severity case, represented by the bold text, was the only severity that was run through the DIC analysis. A full DIC analysis was not performed with either the low or high severity cases. The ARS were used to measure rotational velocity angular acceleration was calculated from measurements taken from the accelerometers. There were six total sensors used: one accelerometer on

the front of the fixture, one accelerometer on the back of the fixture, one ARS on the left of the fixture, one ARS on the right of the fixture, one ARS on the rotational shaft, and one pressure gauge. The pressure gauge was used exclusively for the high severity case. The high severity case consisted of a pneumatic gun that caused movement of the rotational fixture as opposed to the medium and low severity cases which were both driven by gravity. The pneumatic gun was pressurized at 50, 55, 60 and 65 psi which corresponded to specific angular velocities and accelerations.

Table 1: Head Rotation Tests

Severity	Angular Velocity (rad/s)	Angular Acceleration (rad/s^2)
Low	2.15	143
Medium	**3.8**	**477**
High	28	3800

. The heads were separated from the rest of the cadaver by making a separation between the C6 and C7 vertebrae. A custom-designed head alignment tool was used to approximately find the center of rotation of the head. This ensured the proper placement of the head when it was placed in the rotational fixture. Three ARSs were placed on the occipital bone of the head to track the head's motion. Silicone was used to seal the ARSs. To ensure a firm attachment, the occipital bone was ground down in the region of the sensors.

The B-mode ultrasound probe was able to collect 693 images per second at a 40-micron resolution. There were two primary advantages to using B-mode ultrasound: The measurements were noninvasive, and the meningeal layers could be resolved from each other. An example of one of the ultrasound images is shown by Figure 1 located below. The bright white line represents the meningeal layers while the speckled region in the lower portion of the image represents the brain tissue.

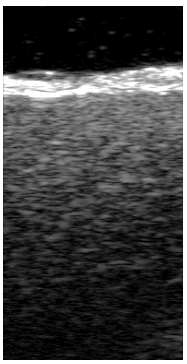

Figure 1: Ultrasound Image

The B-mode ultrasound probe was placed on the center of the left parietal bone. This location was chosen because of a high concentration of bridging veins at this location. To place the probe, a hole was drilled through the bone, and the area around the hole was ground done 1 inch deep to make it easier to place the probe during testing.

The PMHS head was prepared in such a way that it would be physiologically relevant. The head was pressurized with artificial cerebral spinal fluid$^+$ (aCSF$^+$). aCSF$^+$ consisted of artificial cerebral spinal fluid, preservatives, and a dye. An IV bag was used to put the fluid through the internal jugular vein, the common carotid artery, and the vertebral artery. The height of the IV bag was adjusted to get the

pressure within the head to a typical, physiological intracranial pressure (5 – 15 mmHg) (Rangel-Castillo et al.). Additionally, the head was stored at a temperature between 6 and 12 ℃. This was cold enough to minimize brain degradation but not so cold as to change the mechanical properties of the brain tissue. To ensure the temperature of the head did not exit the desire range, noninvasive probes were placed in the ears and the nose. Ice bags were added or removed as needed to control the temperature.

The weight on the fixture was adjusted to control the angular velocity and angular acceleration during low and medium severity testing. Additionally, a pneumatic gun could be used with the rotational fixture to achieve a faster velocity and acceleration. Two accelerometers, three angular rate sensors, and a pressure sensor were attached to the rotation fixture. Tests were done at both low and high speeds with variations between the testing conditions. For low speed testing, the fixture rotated due to the force of gravity only, and no external force was applied. For these tests, a foam padding was placed at the end of the arc of the rotational device to create desired impact pulses: an angular velocity of 2.09-2.15 rad/sec and an angular acceleration of 124-143 rad/sec^2 (Feng et al, 2010). From prior literature, it is known that speeds and accelerations within these ranges do not cause injury to the brain. The medium severity case was defined as 4 times the low severity case. To achieve the medium severity, additional weight was added to the testing apparatus.

2.2 Digital Imaging Correlation

2.2.1 Basic Testing Parameters

Digital Imaging Correlation algorithms — specifically the algorithm used for this study — can track points across a series of images by correlating greyscale coefficient values. The user determines what part of the image to analyze by defining a region of interest (ROI). The algorithm then breaks the ROI down into regions referred to as subsets. Each subset contains points that correspond to pixels of the images of interest. A greyscale value can then be computed for each pixel in the subsequent images, and the greyscale values can then be compared to a reference image. Correlation coefficients are calculated which enable the software to determine which point from a later image likely corresponds to another point from the original image. DIC algorithms then use this information to calculate a deformation vector for each point. Each deformation vector contains information on u displacement, v displacement, and the x and y coordinates. U and v displacement refer to displacement along the x and y axes respectively. Iterative solving methods can then be used to refine the deformation vectors to get more accurate results. The strain can then be approximated from the displacement and coordinate data. All the major parameters for the DIC analysis are dimensionless quantities. The DIC algorithm used for this study calculates a 2D, planar strain which considers deformation in the x and y directions. The DIC test parameters will be discussed more in depth throughout the Methodology section (Blaber et al., 2015).

2.2.2 DIC Software and Installation

To perform the DIC analyses, Ncorr, a MATLAB-compatible software, Ncorr was used. To install Ncorr, a MATLAB compatible C-compiler with OpenMP support was needed. Ncorr's website provided the installation files as C-scripts while MATLAB can only run files as MATLAB Executable files (MEX files). MinGW was used to convert the C-scripts into MEX files that MATLAB could run. MinGW was acquired directly through MATLAB's built in Add-On feature. Once the download of MinGW had finished, the command "mex -setup C++" was used to setup MinGW as the MEX compiler. The installation of Ncorr was continued by typing the command "handles_ncorr = ncorr". At this point, a filepath was set up for

subsequent uses of the Ncorr software. An option was also provided to use OpenMP to select the number of CPU cores to do a multi-CPU core analysis. Due to complications, only 1 CPU core was used for the analyses performed. This will be discussed further in the Discussion section. If desired, the Ncorr files can be manually compiled (Blaber et al., 2017).

2.2.3 Ncorr

2.2.3.1 Main Menu GUI

Once the Ncorr files had been installed, the Ncorr GUI opened to allow for testing setup. The starting GUI is shown in Figure 2(a) located below. The GUI at the end of the analysis is shown by Figure 2(b) located below Figure 2(a).

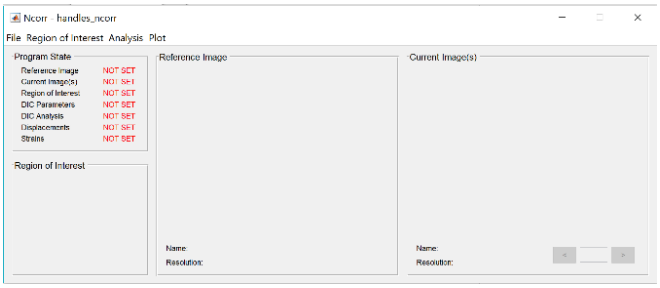

(a)

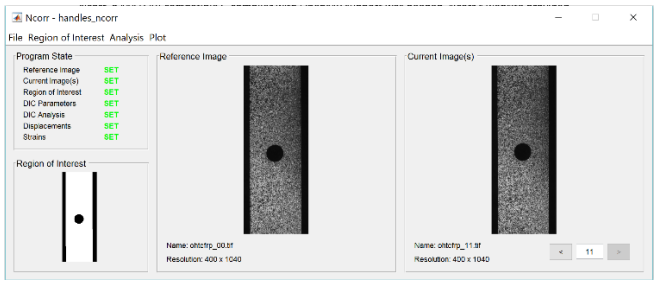

(b)

Figure 2: (a) The main menu GUI for Ncorr before the images have been uploaded. (b) The main menu GUI for Ncorr after uploading the images.

There are a few important features to take note of in the GUI. First, are the six tabs located above: the File tab, the Region of Interest tab, the Analysis tab, and the Plot tab. The file tab allows the user to add reference and current images, output data results to a struct, load data, and clear data. When the reference and current images are uploaded, they appear in their respective windows in the GUI. Each window displays the image file name and the resolution of the image. The current images that appears in the window can be changed with the arrow buttons in the bottom left of the GUI. The filenames of all of the images must be saved in a specific format — filename_#.ext. The "#" symbol and the ".ext" represent the image number and the file extension respectively. This format enables Ncorr to sort the order of the images. Therefore, it does not matter what order the current images are uploaded as Ncorr will sort the images automatically. The Region of Interest tab allows the user to upload an ROI corresponding to an initial image for a forward analysis or an ROI corresponding to a current image for a backward analysis. The selected Region of Interest then appears in the bottom left of the GUI. The Analysis tab allows the user to select the parameters for the DIC analysis. These parameters will be

discussed more in depth in Section 2.2.2.3 The plot tab allows the user to view displacement and strain plots (Blaber et al., 2017).

2.2.3.2 Loading Images

There are three types of images that must be loaded into Ncorr: a reference image, current images, and an ROI. A reference image is the initial image in the sequence. The current images refer to all the other images in the sequence. The ROI, the final type of image, is what is used to determine what points should be analyzed during the DIC analysis. The ROI is a high-contrast image in which the white region corresponds to the points being analyzed and the black region corresponds to the region of the image not being analyzed. A sample ROI that was provided with the Ncorr software is shown by Figure 3 located below. The ROI corresponds with Sample Image 12. Another set of sample images, collectively referred to as Sample 13, was also provided. Sample Image 13 is an object undergoing a high strain test. Sample 13 is represented by Figure 4 located below Figure 3.

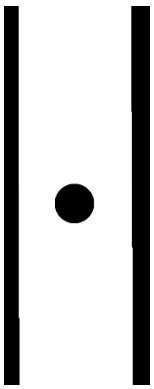

Figure 3: Sample 12 ROI

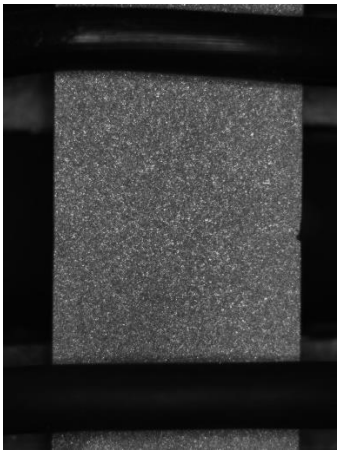

Figure 4: Sample 13

Ncorr can create an ROI if one does not already exist. An ROI can be drawn in either a rectangular, ellipsoidal, or polygonal shape. These drawn regions can be either additive or subtractive for the ROI. For example, the ROI example can be recreated with an additive rectangle for the bulk object and a subtractive ellipse for the hole. The polygon allows for a large variety of shapes, as the user can freely draw the edges of the shape. This option is useful if the region of interest is irregularly shaped. The Ncorr GUI for creating an ROI is shown by Figure 5 located below. (Blaber et al., 2017).

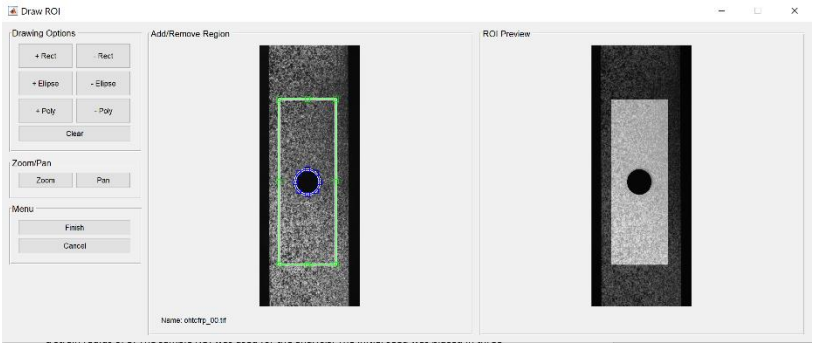

Figure 5: Custom ROI

There are two loading methods for adding current images. These methods are referred to as "Load All" and "Load Lazy". "Load All" loads all the images directly into the Ncorr software. "Load Lazy" only stores the name and filepath of the image. If "Load Lazy" is used, the image files cannot be moved from their original file. The advantage of the "Load Lazy" is that is uses less RAM when performing the analysis (Blaber et al., 2017).

2.2.3.3 Setting DIC Parameters

Before beginning the DIC analysis, the DIC parameters must be set. The two main parameters that are set in this step include the subset radius and the subset spacing. During the DIC analysis, the ROI is broken into individual subunits referred to as subsets. The subsets contain points that correspond to pixels within the image. The subset radius parameter determines the size of an individual subset. It is important to note here that not all DIC algorithms specifically have a subset radius. In the case of Ncorr, the subset is a circle; however, many other DIC algorithms use a square subset. Therefore, subset size is a more encompassing term for the parameter. The subset spacing refers to the spacing between the points within the subset. Ncorr is not limited to making calculations at the pixel level. The digital imaging correlation algorithm can approximate sub-pixel deformation — primarily by an initial guess or seed point — to increase the accuracy of the pixel-level deformation (Blaber et al., 2015).

The DIC Parameter window also allows the user to adjust parameters for the iterative solver. The function of the iterative solver is to find an optimum deformation vector from an initial guess. By default, Ncorr uses the Inverse Compositional Gauss-Newtonian method to balance the accuracy of the final deformation vector with the time taken to sufficiently optimize. Two parameters are involved in the iterative solver: the norm of the difference vector cutoff and the iteration cutoff. For a vector, the norm is equivalent to its magnitude. Therefore, the norm of a difference vector is the same as the distance between two points. Figure 6, located on the next page, illustrates the concept of the norm of a difference vector (Blaber et al., 2015).

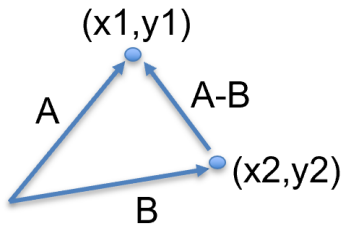

Figure 6: Norm of the Difference Vector

If desired, the iteration cutoff can be reduced, or the norm of the difference vector can be increased to reduce the computational time. By default, the norm of the difference vector cutoff is set to $1*10^{-6}$, and the iteration cutoff is set to 50 (Blaber et al., 2015).

Two other important features are in the DIC Parameters window. First is the High Strain Analysis feature. The High Strain Analysis feature makes it possible to change the reference image in the analysis. Additionally, the High Strain Analysis makes it possible to make multiple initial guesses throughout the analysis. Normally, only one initial guess, also referred to as a seed, is made at the start of the analysis. There are two options for making additional initial guesses. If "Seed Propagation" is selected, a new seed will be placed every time the correlation coefficient becomes abnormally large. If "Leapfrog" is selected, a step-parameter can be defined to set a new seed after a certain number of images. The other important feature of the DIC Parameters window is the Discontinuous Analysis option. This feature is used if there is an abrupt discontinuity between images such as in the case of crack propagation (Blaber et al., 2015). The DIC Parameters is represented by Figure 7 located below.

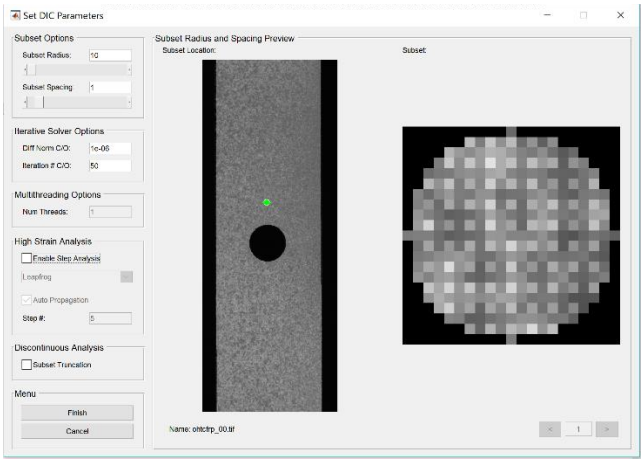

Figure 7: DIC Parameters Window

2.2.3.4 Initial Guess

At this point, the user can then set an initial guess for the DIC analysis. First a region for the seed (initial guess) to be placed must be selected. This part of the testing is where the OpenMP support becomes important. If multiple CPU cores are used for the analysis, the ROI can be split into multiple regions, and multiple initial guesses can be used. For all the analyses in this study, only one region was used (Blaber et al. 2015). The select region window is shown on the next page by Figure 8.

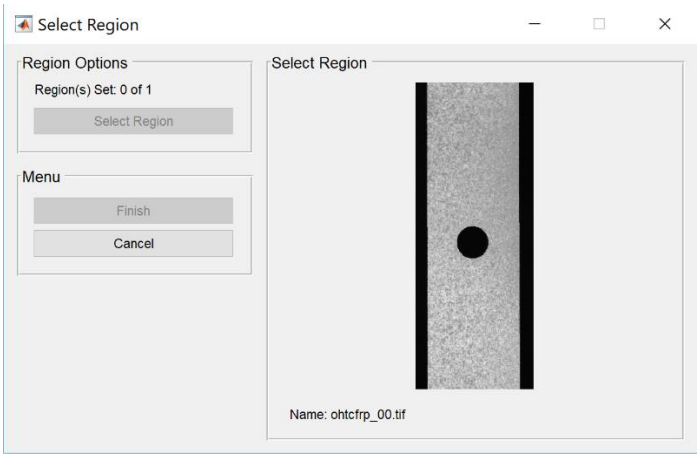

Figure 8: Select Region Window

An option is then given to place the seed. Care should be taken when placing the seed because all the subsequent calculations are based on the initial guess. According to documentation, the seed placement becomes more important as an object undergoes high amounts of strain. Additionally, the initial guess should not be placed in a region that exits the ROI or the boundaries of the images over time. Documentation also shows that the placement of the seed is important for calculating subpixel deformation. While Ncorr does not output data for subpixel deformation, a good calculation for subpixel deformation should theoretically increase the accuracy of pixel-level deformation. (Blaber et al., 2015). The placement of the seed is shown by Figure 9 located below.

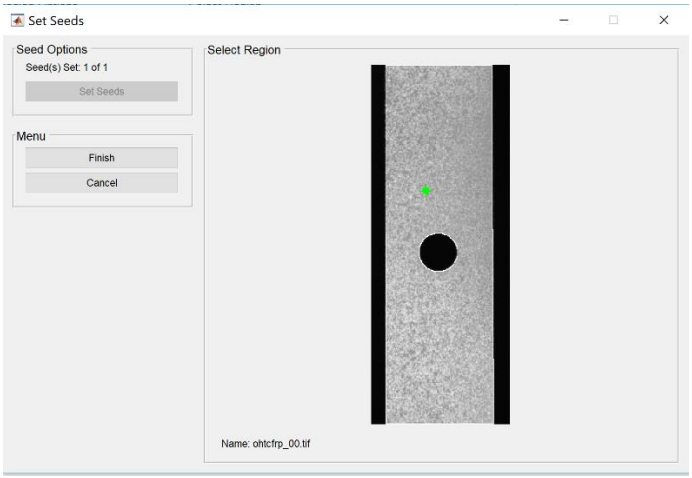

Figure 9: Seed Window

After the seed is placed, Ncorr displays a window that shows a brief preview of the analysis. The most important information in the preview window includes the numbers of iterations and the correlation coefficient values for the images. The iteration number should be low. If the iteration value is high, the deformation vector likely did not optimize properly during the analysis. If the iteration number is the same as the iteration cutoff, the analysis likely failed. The correlation coefficient displayed should be relatively close to zero. If it is not close to zero, an error occurred during the analysis. The window is shown below (Blaber et al., 2017). The Seed Preview window is shown by Figure 10 located at the top of the next page.

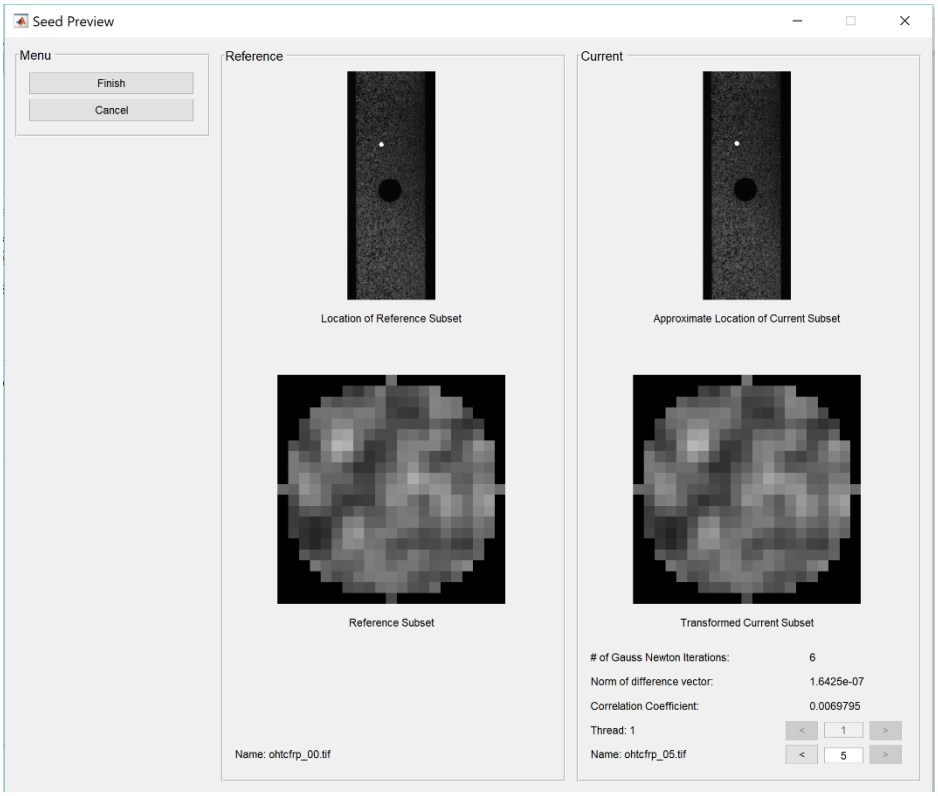

Figure 10: Seed Preview Window

2.2.3.4 Formatting Displacement Data

Once the seed has been placed, additional information must be entered into the Format Displacement window to convert the displacement calculations into an applicable measurement. This is similar to other imaging software in that it requires a pixel to unit conversion factor. In other words, the dimensions of the object must be known to get the final displacement values. The window also provides an option to exclude points from the graph that have high correlation coefficient values. If the image has lens distortion from the camera used, that can be considered here as well (Blaber et al., 2017). The Format Displacements window is shown by Figure 11 located below.

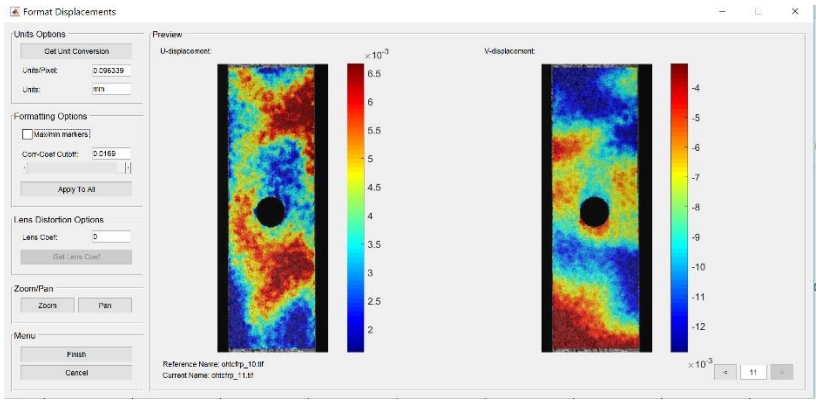

Figure 11: Format Displacements Window

2.2.3.5 Calculating Strains

Ncorr's DIC algorithm calculates 2D (planar) strain. Equations 1-3, shown below, are used to calculate planar strain.

$$\textit{Equation 1: } Exx = \frac{1}{2} * (2 * \frac{\partial u}{\partial x} + (\frac{\partial u}{\partial x})^2 + \left(\frac{\partial v}{\partial x}\right)^2)$$

$$\textit{Equation 2: } Exy = \frac{1}{2} * (\frac{\partial u}{\partial y} + \frac{\partial v}{\partial x} + \frac{\partial u}{\partial x}\frac{\partial u}{\partial y} + \frac{\partial v}{\partial x}\frac{\partial v}{\partial y})$$

$$\textit{Equation 3: } Eyy = \frac{1}{2} * (2 * \frac{\partial v}{\partial y} + (\frac{\partial u}{\partial y})^2 + (\frac{\partial v}{\partial y})^2)$$

For small regions, the gradient of displacement with respect to the x and y coordinates can be approximated by fitting a plane to the data. This is done twice: once for the u displacement and once for the v displacement. The plane equations for both u displacement and v displacement are shown by Equations 4 and 5 which are shown below.

$$\textit{Equation 4: } u(i,j) = a_0 + a_1 x + a_2 y$$

$$\textit{Equation 5: } v(i,j) = b_0 + b_1 x + b_2 y$$

It is important to note here that a_1, a_2, b_1 and b_2 correspond to the partial derivates of the displacement with respect to the coordinate points. Therefore, the plane equations can be rewritten as Equations 6 and 7 which are shown below.

$$\textit{Equation 6: } u(i,j) = a_u + \left(\frac{\partial u}{\partial x}\right) x + \left(\frac{\partial u}{\partial y}\right) y$$

$$\textit{Equation 7: } v(i,j) = a_v + \left(\frac{\partial v}{\partial x}\right) x + \left(\frac{\partial v}{\partial y}\right) y$$

The variables a_u and a_v represent the intersection of the plane with the z axis for the u-displacement and v-displacement planes respectively (Pan et al., 2009). Figure 12(a), an example of a good fit, and Figure 12(b), an example of a bad fit, are located below.

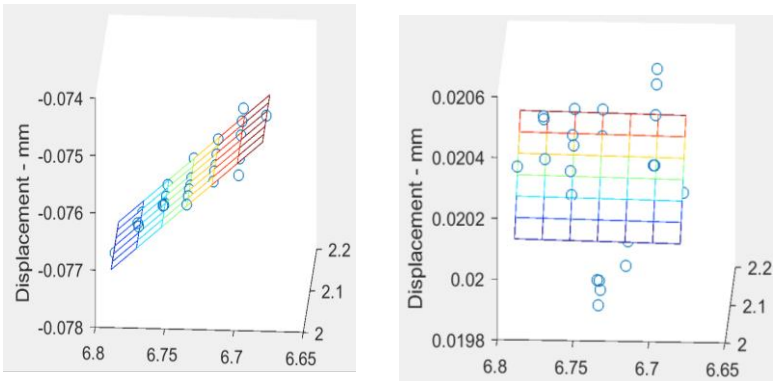

(a) *(b)*

Figure 12: (a) An example of a good fit for the plane fitted to the displacement data for strain calculations. (b) An example of a bad fit for the plane fitted to the displacement data for strain calculations.

It is desirable for the points to be directly on the surface of the plane such as in Figure 12(a). In Figure 12(b), the plane is in a different orientation, and the points are located away from the surface of the plane (Blaber et al., 2015).

2.2.2.6 Interpreting Plots

At the end of the analysis, Ncorr provides plots for u displacement, v displacement, Exx strain, Exy strain, and Eyy strain. Figure 13, located below, shows the plot window.

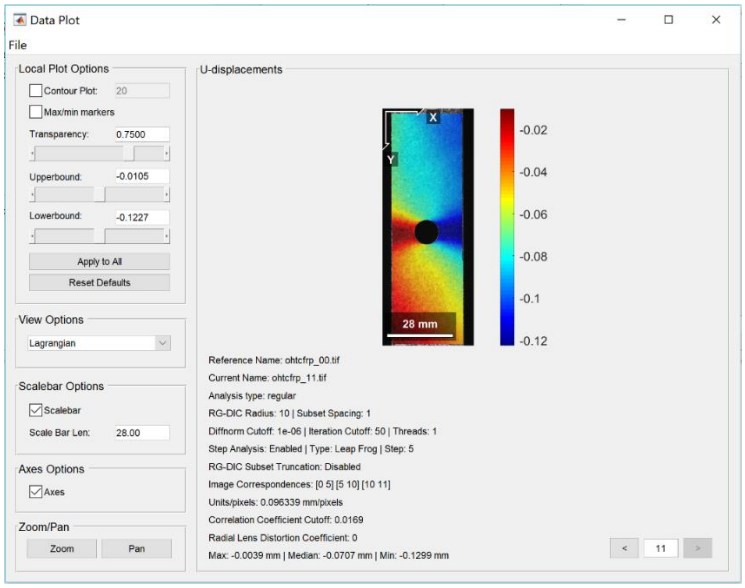

Figure 13: Plot Example

Additionally, the user can switch between Green-Lagrangian and Eulerian-Almansi strain; however, for the purpose of the analyses done in this report, only Eulerian-Almansi strain was analyzed. The file tab within plot window also allows the user to save the image as a GIF to see the change in displacement and strain over time. Additionally, Ncorr displays the maximum, minimum, and median displacement or strain value for each image in the series. An example of the plot window is shown below. A scalebar can be defined to make it easier to visualize the physical dimensions of the object in the image. If desired, the plot can also be viewed as a contour plot. The transparency of the plot and the boundaries of the scalebar can also be adjusted (Blaber et al., 2017).

2.3 Digital Imaging Correlation Parametric Studies

The DIC testing parameters were varied one at a time to study the effects on the analysis. All parametric studies mentioned in this section were performed on Sample 12, a set of sample images from Ncorr's website. Sample 12 consisted of 11 images and a sample ROI. For an example of one of the sample images, refer to Figure 3. These parameters included the position of seed (initial guess), the subset spacing size, the subset radius size, the strain radius size, and the strain radius placement. The sample consisted of a piece of metal with a hole in the center. The Lazy Loading method mentioned earlier was used to load all current images to conserve RAM. All sample images were 400 x 1040 pixels with an assumed width of 30 mm. This gave a pixel to unit conversion of 0.096339 mm/pixel. Additionally, all parametric study tests used the default values for the iterative solver from the Inverse Compositional Gauss-Newtonian method.

2.3.1 Effect of Seed Placement

For the seed placement test, the following parameters were used: a subset radius of 10, a subset spacing of 1, and a strain radius of 3. The sample ROI for Sample 12 that was provided by Ncorr's website was used for the analysis. The initial seed was placed in three separate locations: one in the middle of the object, one at the lower edge of the ROI of the object, and one next to the hole in the center of the object. All three testing setups are shown by Figures 14(a) through 14(c) located below.

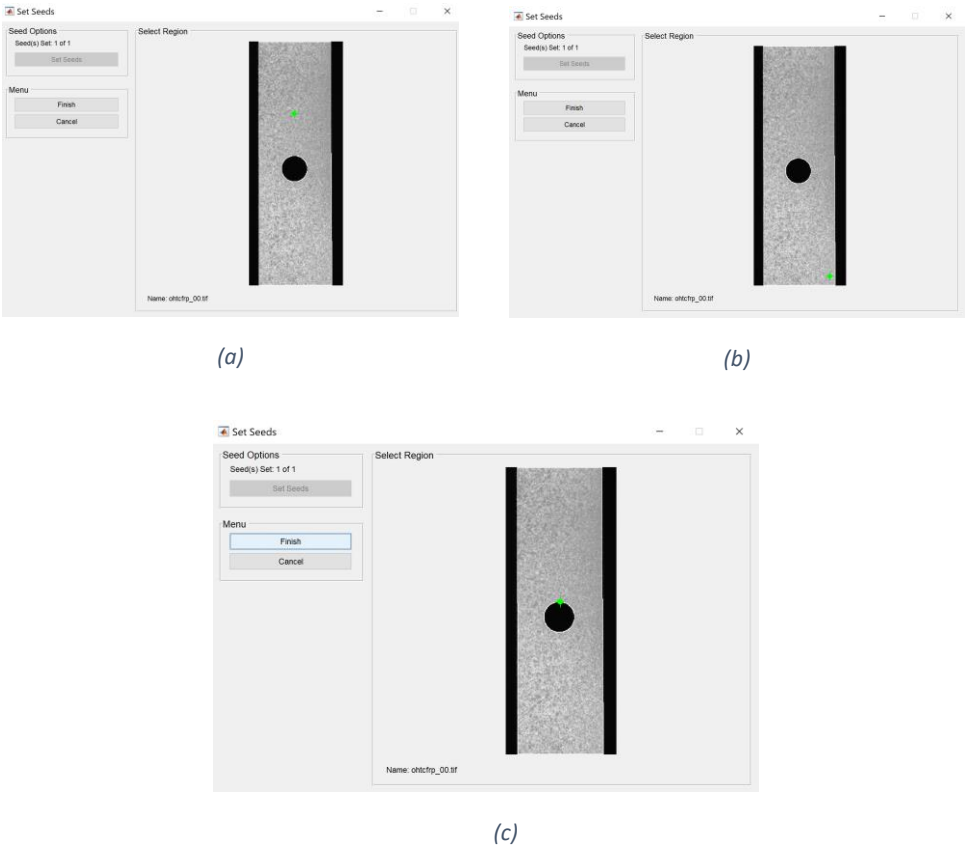

Figure 14: (a) The location of the first seed. (b) The location of the second seed. (c) The location of the third seed.

It was assumed that if the seed placement were to have an effect, it would be most likely to have an effect near the boundaries of the ROI. That is why one seed was placed at the bottom and one seed was placed on the boundary of the hole.

2.3.2 Effect of Subset Spacing

For the subset spacing test, a subset radius of 10 and a strain radius of 3 were used. Seed placement 1, shown by Figure 14(a), was used. The sample ROI provided by Ncorr's website was also used for the analysis. To minimize confounding variables, a constant strain window position was used for each subset spacing. This was approximately 7-8 mm to the left of the hole halfway down the sample. Four different subset spacings were used: 0, 1, 5, and 10. The range of available subset spacing values ranged from 0-10. The subset spacing of 0 was especially of interest as that would seem to imply that there was no spacing between the points.

2.3.3 Effect of Subset Radius

For the subset radius test, the following parameters were used: a subset spacing of 3, a strain radius of 3, and the default values of the norm of the difference vector cutoff and the iteration cutoff. The seed placement and strain radius placement were the same as the subset spacing test. Eight different subset spacings were tested: 10, 12, 14, 16, 18 ,20, 22, and 24. Unlike the subset spacing test, this did not include the entire range of available values. This was primarily because the subset radius could be increased up to a value of 60. It was assumed that a general relationship between the subset radius and the displacement and strain results with only part of the range of subset radius values.

2.3.4 Effect of Strain Radius

A subset radius of 10 and a subset spacing of 1 were used for the strain radius test. Seed placement 1 was used. The strain radius was placed 7 to 8 mm to the left of the hole in the center of the object. Three different strain radius values were tested for this study: 3, 30, and 50. A strain radius of 3 was used as a control. A strain radius of 3 provided a good fit for accurate strain calculations. A strain radius of 30 and 50 appeared to cause a bad fit that would likely affect the calculations. Both the fit and the strain plots were analyzed to see how a change in the strain radius affected the quality of the results.

2.3.5 Effect of Strain Window Placement

The following parameters were used for the strain window placement test: a subset spacing of 10, a subset radius of 10, and a strain radius of 3. The strain window was placed in three different locations: above the hole in the center, at the bottom of the ROI, and on the edge of the hole in the center of the object. The three test conditions are shown by Figures 15(a), 15(b), 16(a), 16(b), 17(a) and 17(b) located below and on the next page. The plane used for each strain calculation is also shown. The plane fitted to the u displacement data and the plane fitted to the v displacement data are shown for each strain window placement.

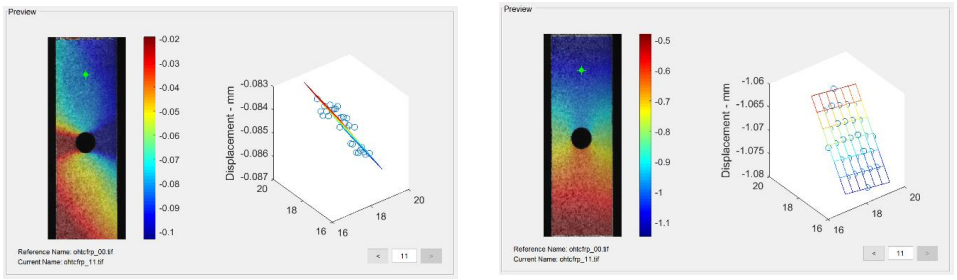

(a) *(b)*

Figure 15: (a) The effect of the first strain window placement on the plane fitted to the U displacement data. (b) The effect of the first strain window placement on the plane fitted to the U displacement data.

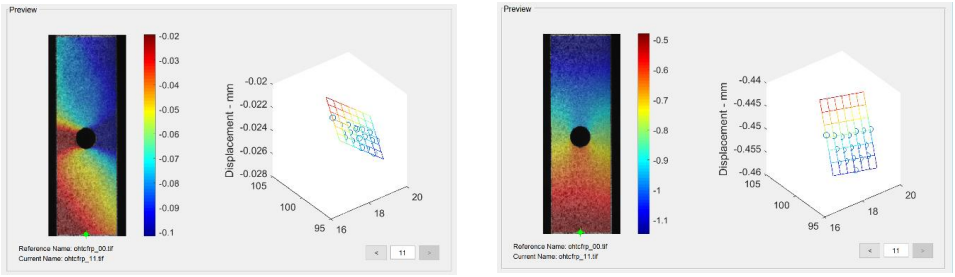

(a) *(b)*

Figure 16: (a) The effect of the second strain window placement on the plane fitted to the U displacement data. (b) The effect of the second strain window placement on the plane fitted to the V displacement data.

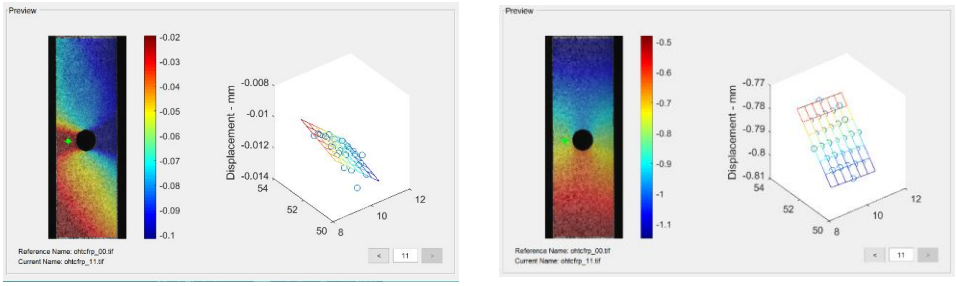

(a) *(b)*

Figure 17: (a) The effect of the third strain window placement on the plane fit to the u displacement data. (b) The effect of the third strain window placement on the plane fit to the v displacement data.

The logic for this test was similar to that of the seed placement test. It was hypothesized that if the strain window placement had an effect, the effect would be most likely to occur near the boundaries of Sample 12's ROI.

2.4 High Strain Analysis

2.4.1 Validation Test

A validation test was performed to see if the high strain analysis settings would give valid results. This test was necessary as the high strain analysis settings would likely be necessary to analyze the high severity ultrasound images. Sample 12 from Ncorr's website was used for the analysis. To test the validity of the analysis, an analysis that used the Sample 12 images was performed using both the high strain analysis settings and the normal analysis settings. The parameters used included a subset radius of 10, and a subset spacing of 1. Seed placement 1 was used, and the strain radius was placed 7 to 8 mm to the left of the hole in the center of the object. For the high strain analysis, Auto-Propagation was used with a Leapfrog step-parameter of 5. The high strain analysis parameters were chosen to see if making repeated initial guesses would affect the calculations if a new initial guess was not necessary.

2.4.2 Normal Analysis on High Strain Images

An analysis was run to see if the high strain analysis was necessary for high strain images. Sample 13, a set of images involving an object undergoing high strain, from Ncorr's website was used for the analysis. Sample 13 is shown by Figure 4 at the beginning of the report. The testing parameters used included a subset spacing of 1, a subset radius of 10, and a strain radius of 3. If successful, the normal analysis on the high strain image would then be compared to a high strain analysis of the same set of images.

2.4.3 High Strain Analysis on High Strain Images

The goal of this test was to study the different parameters of the high strain analysis. The parameters included the auto-propagation setting, the Leapfrog setting, and the manual seed placement setting. Like the previous high strain test, Sample 13, shown by Figure 4, was analyzed for this analysis. Unfortunately, the high strain analysis was unable to be completed on the high strain image with any combination of settings. For more information, see the results section.

2.5 Effect of ROI on Ultrasound Image Analysis

Before performing an optimum parameter analysis on the ultrasound images, a test was performed on the medium severity images to determine the best ROI for the optimum parameter analysis. Four ROIs were used: a 1mm wide and 3mm tall ROI that was 1 mm to the left of the center of the image, a 1 mm wide and 3 mm tall ROI that was directly in the center of the image, a 3 mm wide and 1 mm tall ROI that was against the bottom of the brain tissue in the ultrasound image and a 3 mm wide and 1 mm tall ROI that was against the meninges of the brain tissue in the ultrasound image. The four ROIs that were used are shown at the end of this paragraph by Figures 18(a) through 18(d).

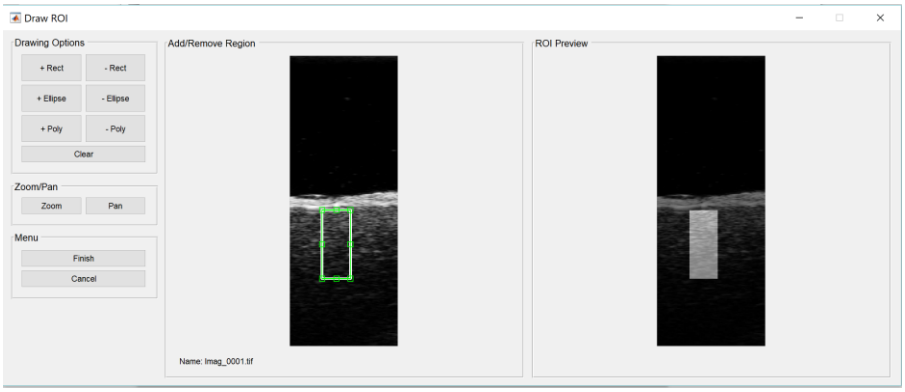

(a)

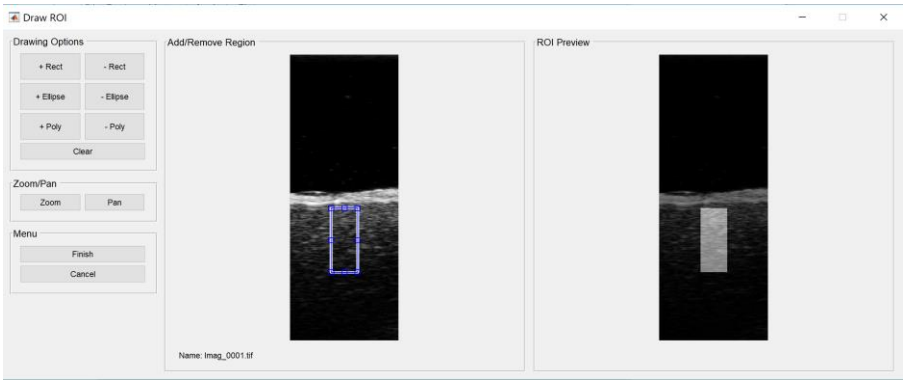

(b)

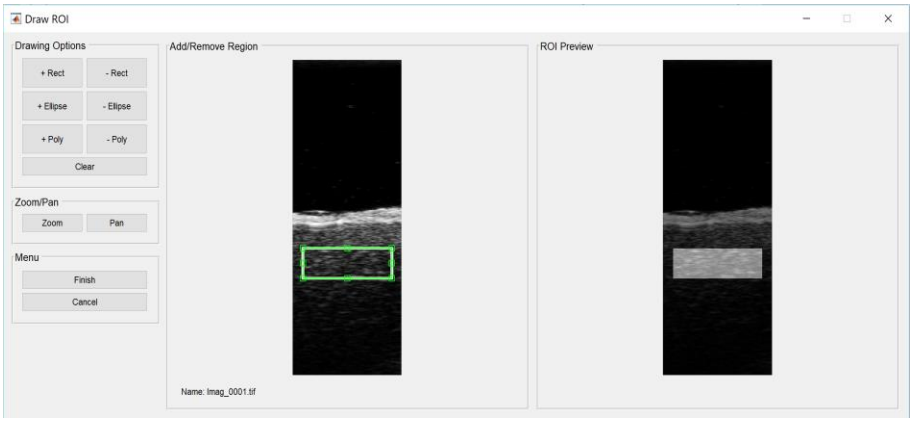

(c)

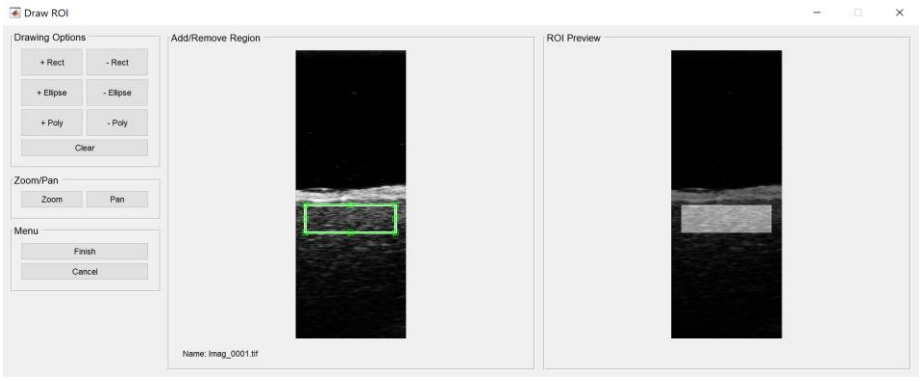

(d)

Figure 18: (a) The shape and placement of the first ROI. (b) The shape and placement of the second ROI. (c) The shape and placement of the third ROI. (d) The shape and placement of the fourth ROI.

The purpose of this study was to see if the shape or the placement had a noticeable effect on the ROI. Only the strain plots were analyzed for this specific test. The seed placement for all the ROIs was in the center of the ROI. The other DIC parameters used for this study included a subset radius of 10, a subset

spacing of 1, and a strain radius of 2. Each image had a resolution of 224 x 600 pixels and an approximate width of 4 mm. This gave a pixel to unit conversion factor of 0.0182 mm/pixel.

2.6 Ultrasound Image Optimum Parameter Analysis

From the results of the parametric studies, optimum parameters were chosen for each setting: a subset spacing of 3, a subset radius of 20, and a strain radius of 3. For more information on why these parameters were chosen for the Optimum Parameter analysis, seed sections 3.2, 3.3, and 3.4. The default values for the norm of the difference vector cutoff and the iteration cutoff were used. ROI 2, represented by Figure 18(b), from the ROI test was used for the analysis. ROI 2 was chosen because it made it possible to view displacement and strain at varying depths. The displacement and strain will vary between different depths in the brain tissue. Therefore, an injury could occur at one depth but not another depth. It was also thought that placing the ROI in the center of the image would make it easier to track the shear motion. If the ROI were not placed in the center of the image, the entire right half of the image would be ignored. For more information on this, see Section 3.7. Both the seed and strain window were placed in the center of the ROI. More ultrasound images were collected than were needed for the analysis. All ultrasound images that did not represent the desired head motion — the displacement of the head from the beginning to the end of the predetermined arc length — were excluded from the analysis. A total of 171 images were collected, but only images 10-60 were used in the analysis. Three displacement values were also obtained from the image with the maximum displacement value. The values were taken at the surface of the brain tissue, 1 mm deep in the brain tissue, and 2 mm deep in the brain tissue. The displacement values were then compared to similar displacement values taken from an analysis in TEMA. TEMA is a point tracking software that is commonly used in Injury Biomechanics.

2.7 Effect of Subset Radius on Noise

The strain plots from the study mentioned in Section 2.6 had noise that made it impossible to interpret the data. See Section 3.8 within the results section for a further justification of this specific test. Information was found that indicated that the size of a subset affects the amount of noise in the data. This was based on the analysis of the subset radius test in Section 3.3.8. The original subset radius test was limited by not doing the full range of subset radius values. It was determined that another study should be done with ROI 2, represented by Figure 18(b), to see if increasing the subset radius would minimize the noise from the analysis of the ultrasound image. The analysis was split into two segments with two different scale bars. This was done to see the effects on the noise at larger and smaller scales. A subset radius of 2 and a subset spacing of 2 were used for the analysis. The seed and strain radius were both placed in the center of the ROI.

Chapter 3: Results

3.1 Effect of Seed Placement

Figures 19(a) through 19(c), 20(a) through 20(c) and 21(a) through 21(c), shown on the next two pages, show the results from the seed placement test. Each row of images corresponds to a different type of strain: Images 19(a) through 19(c) correspond to Exx strain, images 21(a) through 20(c) correspond to Exy strain, and images 21(a) through 21(c) correspond to Eyy strain.

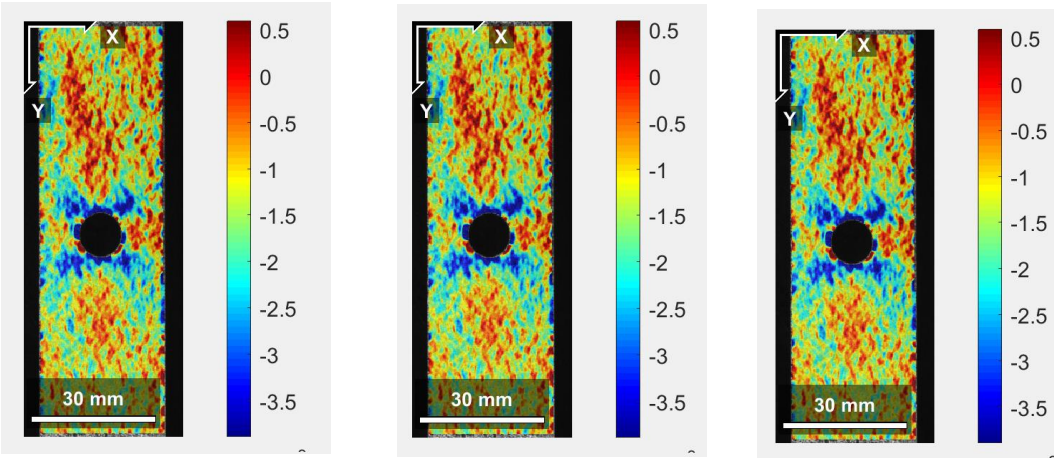

(a) *(b)* *(c)*

Figure 19: (a) The effect of the first seed placement on Exx strain. (b) The effect of the second seed placement on Exx strain. (c) The effect of the third seed placement on Exx strain.

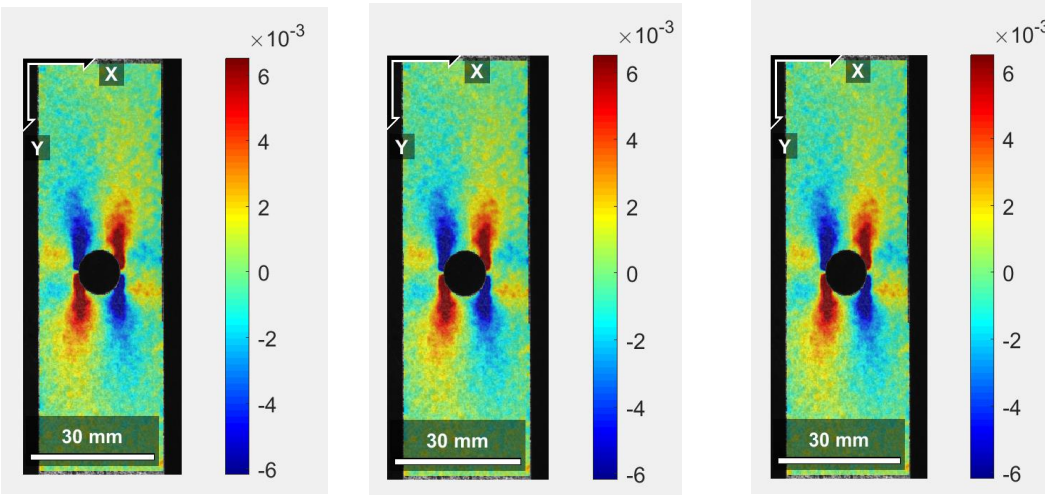

(a) *(b)* *(c)*

Figure 20: (a) The effect of the first seed placement on Exy strain. (b) The effect of the second seed placement on Exy strain. (c) The effect of the third seed placement on Exy strain.

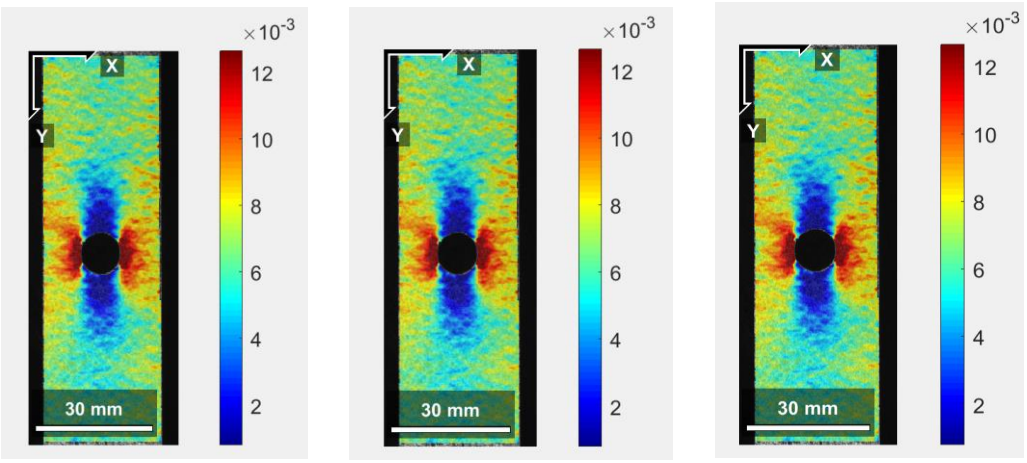

(a) *(b)* *(c)*

Figure 21: (a) The effect of the first seed placement on Eyy strain. (b) The effect of the second seed placement on Eyy strain. (c) The effect of the third seed placement on Eyy strain.

From the analysis, the seed placement had no impact on the results. For Exx strain, Exy strain and Eyy strain, the placement of the seed did not change the strain plot. This is shown by how each row has three identical images. This was surprising as the initial guess is important in completing the analysis. It is likely because images analyzed underwent a relatively small amount of strain for each image. It is possible that a higher strain rate could increase the importance of the seed placement. It was also surprising that placing the seed close to the boundaries of the ROI had not effect. However, it is possible that the strain rate was low enough that boundaries of the ROI had no major significance on the analysis. This study should be repeated on a high strain image to see if the seep placement becomes more important.

3.2 Effect of Subset Spacing

Figures 22(a) through 22(d), 23(a) through 23(d) and 24(a) through 24(d), located on the next two pages, show the results of the subset spacing test. The arrangement of the images is similar to the arrangement for the seed placement test. The rows correspond to Exx strain, Exy strain and Eyy strain. Each row arranges the images in order of increasing subset spacing: The subset spacings that were tested include 0, 1, 5 and 10.

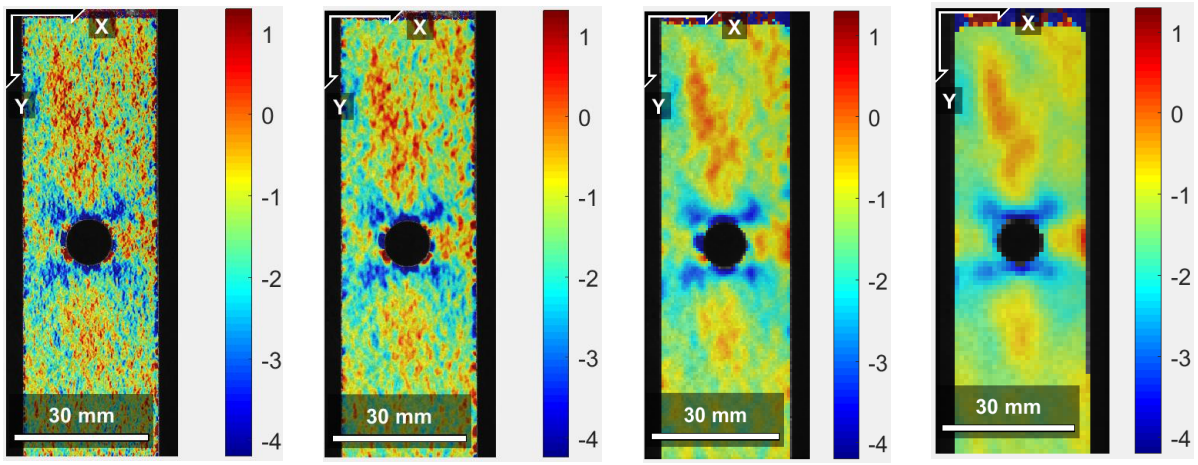

(a) *(b)* *(c)* *(d)*

Figure 22: (a) The effect of a subset spacing of zero on Exx strain. (b) The effect of a subset spacing of 1 on Exx strain. (c) The effect of a subset spacing of 5 on Exx strain. (d) The effect of a subset spacing of 10 on Exx strain.

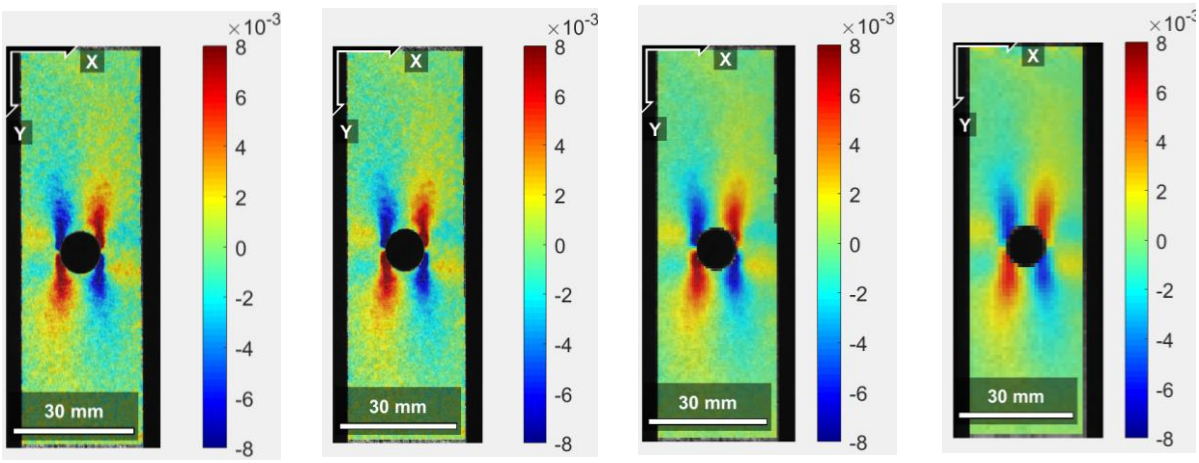

(a) *(b)* *(c)* *(d)*

Figure 23: (a) The effect of a subset spacing of zero on Exy strain. (b) The effect of a subset spacing of 1 on Exy strain. (c) The effect of a subset spacing of 5 on Exy strain. (d) The effect of a subset spacing of 10 on Exy strain.

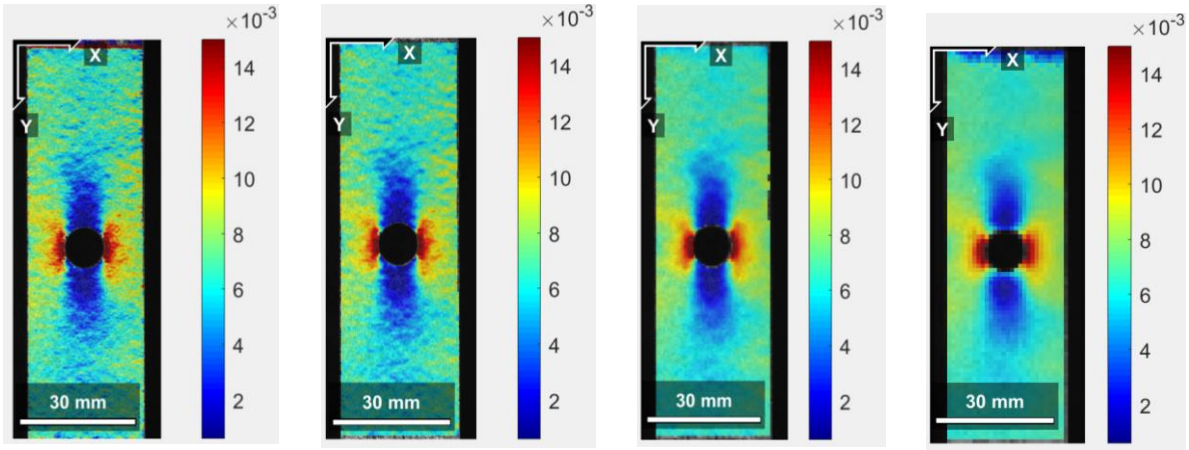

Figure 24: (a) The effect of a subset spacing of 0 on Eyy strain. (b) The effect of a subset spacing of 1 on Exy strain. (c) The effect of a subset spacing of 5 on Eyy strain. (d) The effect of a subset spacing of 10 on Eyy strain.

For the subset spacing test, there was a noticeable impact on the resolution of the plots. The images became blurrier as the subset spacing increased. Upon further research, it was discovered that the subset spacing parameter changes the spacing between points by converting the image into a lower resolution and reducing the number of pixels in the image. (Blaber et al., 2015) Therefore, with a larger subset spacing, the total number of analyzed points decreases and the spacing between the individual points increases. After saving the data from Ncorr as a struct, the number of points analyzed for each image were compared. An equation was then derived that related the number of points in an image and the subset spacing. This equation is represented by Equation 8 which is shown below.

$$Equation\ 8: Resolution_{out} = Resolution_{in} * (\frac{1}{n+1})$$

In the equation, n corresponds to the magnitude of the subset spacing. A value of 0 for the subset spacing implies that the resolution of the image does not change. With a value of 1 for the subset spacing, the resolution for the image is already half of the original resolution.

From the results it was determined that a small change in the subset spacing had a relatively small impact on the strain calculations. For example, between Figure 22(a) and Figure 22(b) for the Exx strain, the plots were similar. Even though Figure 22(b) had half the resolution of Figure 22(a), the plots gave essentially the same information. Therefore, it was determined that a very low subset resolution would be unnecessary for the ultrasound image analysis. It was decided that a subset spacing of 3 would provide a good balance between the resolution of the plots and the computation load of the analysis.

3.3 Effect of Subset Radius

3.3.1 U Displacement

Figures 25(a) through 25(h), located on the next two pages, represent the plots for u displacement. The images are arranged by an increasing subset radius. The subset radius values that were tested were 10, 12, 14, 16, 18, 20, 22, and 24.

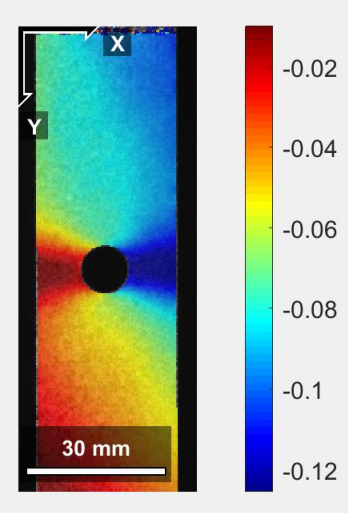
X
Y
30 mm
-0.02
-0.04
-0.06
-0.08
-0.1
-0.12

(a)

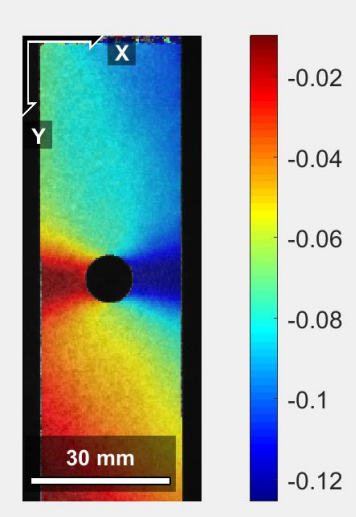
X
Y
30 mm
-0.02
-0.04
-0.06
-0.08
-0.1
-0.12

(b)

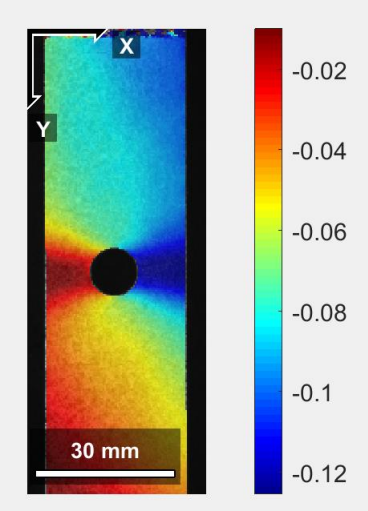
X
Y
30 mm
-0.02
-0.04
-0.06
-0.08
-0.1
-0.12

(c)

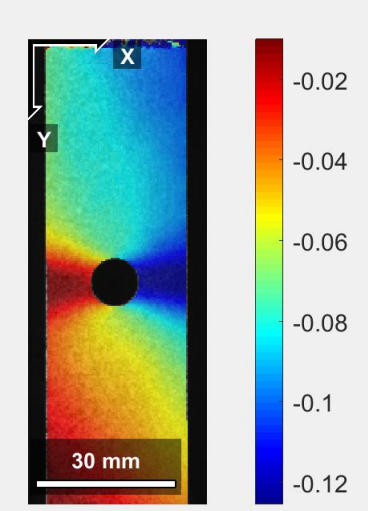
X
Y
30 mm
-0.02
-0.04
-0.06
-0.08
-0.1
-0.12

(d)

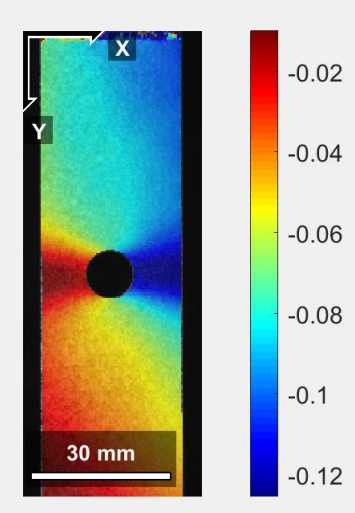
X
Y
30 mm
-0.02
-0.04
-0.06
-0.08
-0.1
-0.12

(e)

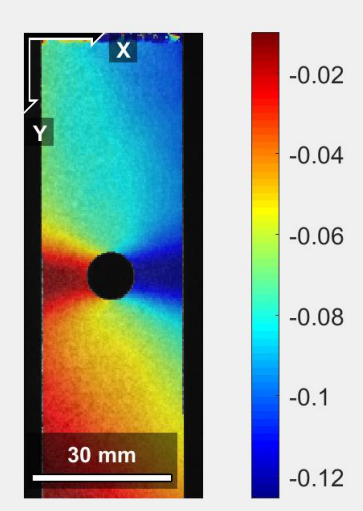
X
Y
30 mm
-0.02
-0.04
-0.06
-0.08
-0.1
-0.12

(f)

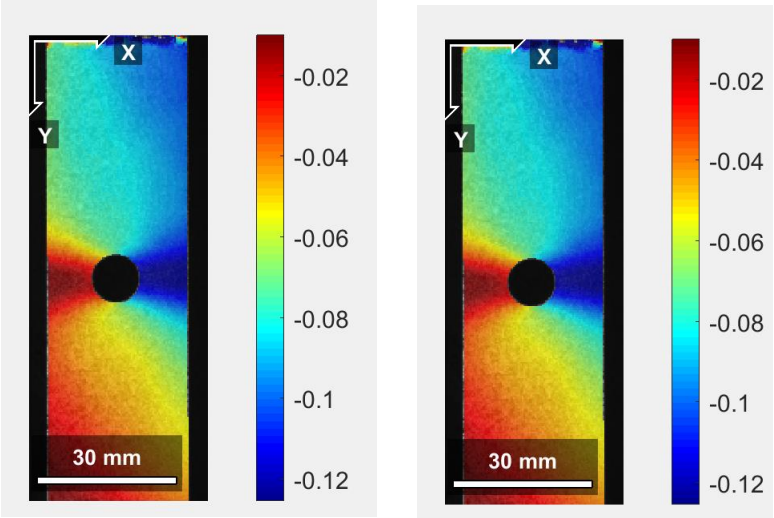

(g) *(h)*

Figure 25: (a) The effect of a subset radius of 10 on u displacement. (b) The effect of a subset radius of 12 on u displacement. (c) The effect of a subset radius of 14 on u displacement. (d) The effect of a subset radius of 16 on u displacement. (e) The effect of a subset radius of 18 on u displacement. (f) The effect of a subset radius of 20 on u displacement. (g) The effect of a subset radius of 22 on u displacement. (h) the effect of a subset radius of 24 on u displacement.

There did not appear to be any effect on the u displacement calculations based on looking at the plots. For the low strain images, there does not appear to be a significant effect on the calculations.

3.3.2 V Displacement

Figures 26(a) through 26(h), located below and on the next page, represent the plots for u displacement. The images are arranged by an increasing subset radius. The subset radius values that were tested were 10, 12, 14, 16, 18, 20, 22, and 24.

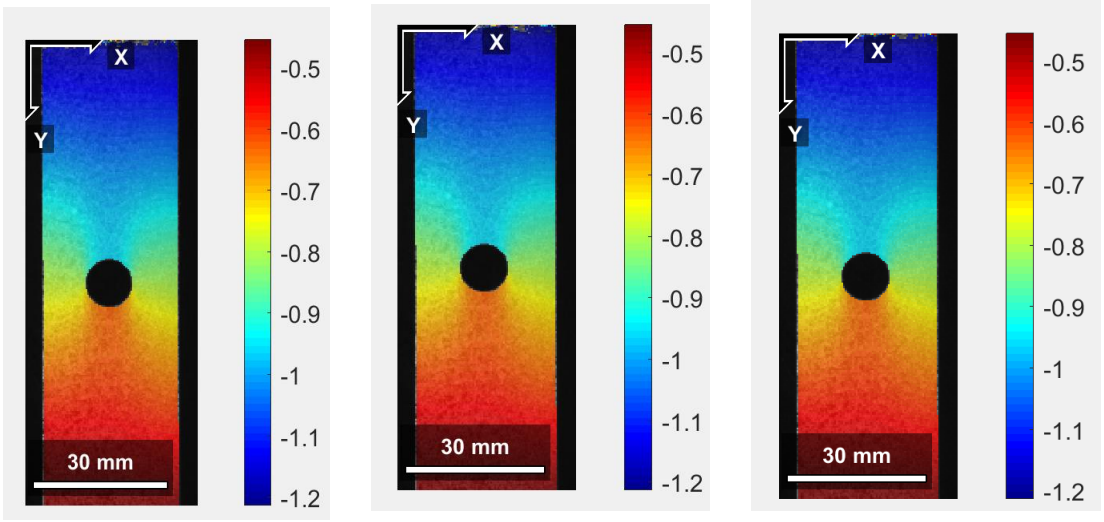

(a) *(b)* *(c)*

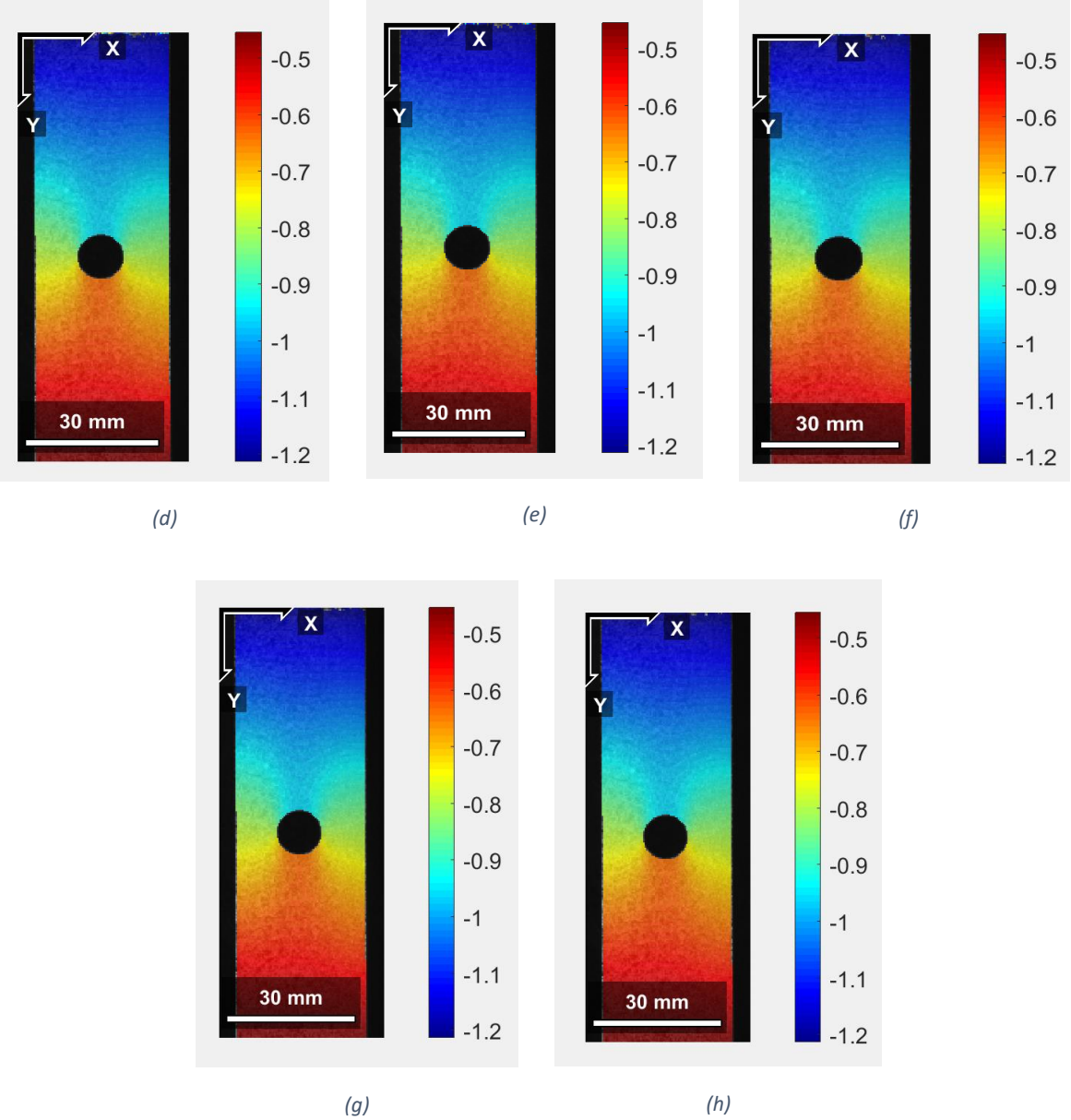

Figure 26: (a) The effect of a subset radius of 10 on v displacement. (b) The effect of a subset radius of 12 on v displacement. (c) The effect of a subset radius of 14 on v displacement. (d) The effect of a subset radius of 16 on v displacement. (e) The effect of a subset radius of 18 on v displacement. (f) The effect of a subset radius of 20 on v displacement. (g) The effect of a subset radius of 22 on v displacement. (h) the effect of a subset radius of 24 on v displacement.

Similar to the u displacement plots, there did not appear to be any effect on the v displacement calculations based on changing the subset radius. For the low strain images, there does not appear to be a significant effect on the calculations.

3.3.3 U-Displacement Plane

Figures 27(a) through 27(h), located below and on the next page, show how a change in the subset radius affects the fit of the plane applied to the u displacement data for the strain calculations. The images are arranged by an increasing subset radius. The subset radius values that were tested were 10, 12, 14, 16, 18, 20, 22, and 24.

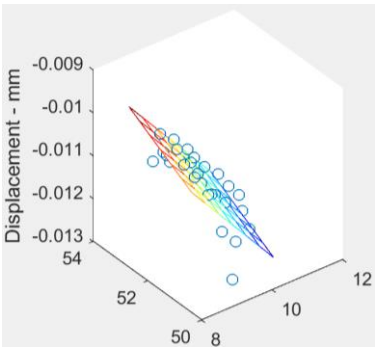

(a)

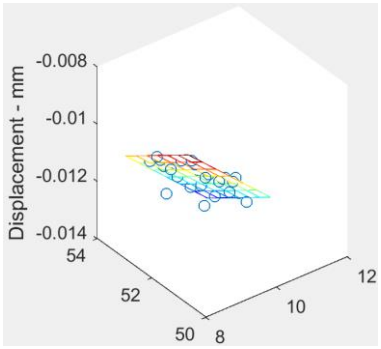

(b)

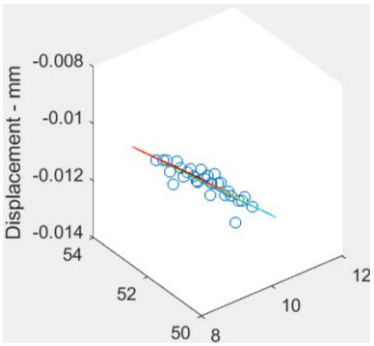

(c)

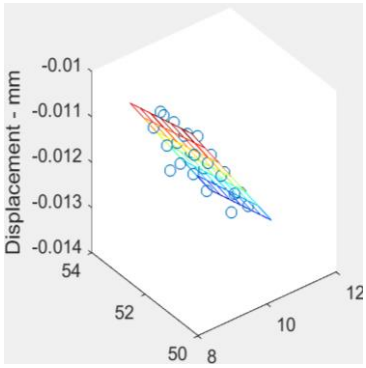

(d)

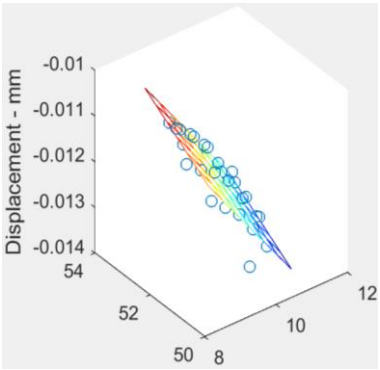

(e)

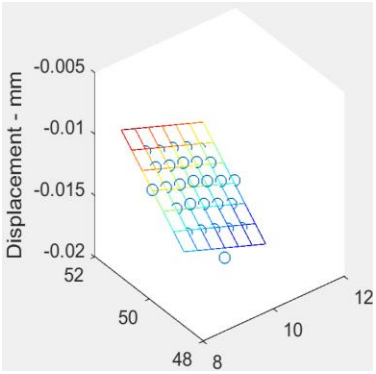

(f)

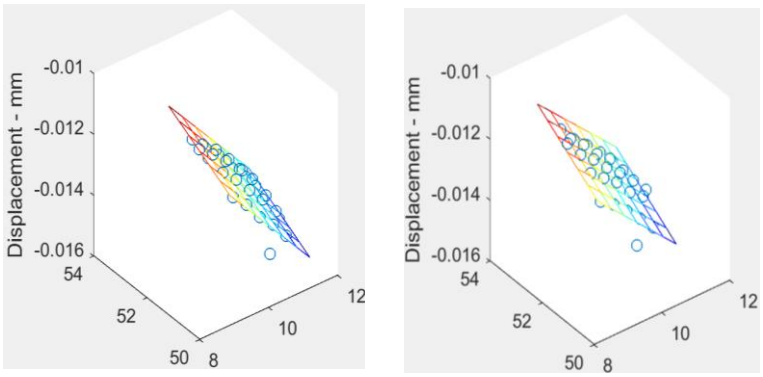

(g) *(h)*

Figure 27: (a) Subset radius 10 u displacement plane. (b) Subset radius 12 u displacement plane. (c) Subset radius 14 u displacement plane. (d) Subset radius 16 u displacement plane. (e) Subset radius of 18 u displacement plane. (f) Subset radius 20 u displacement plane. (g) Subset radius 22 u displacement plane. (h) Subset radius 24 u displacement plane.

An increase in the subset radius appeared to cause a better fit with the plane use for the strain calculations. This observation was based on a qualitative analysis. This can best be observed by comparing Figure 27(a) and Figure 27(f). In Figure 27(a), there are multiple points that are located away from the surface of the plane. However, in figure 27(f), the points are flusher against the surface of the plane.

3.3.4 V-Displacement Plane

Figures 28(a) through 28(h), located below and on the next page, show how a change in the subset radius affects the fit of the plane applied to the v displacement data for the strain calculations. The images are arranged by an increasing subset radius. The subset radius values that were tested were 10, 12, 14, 16, 18, 20, 22, and 24.

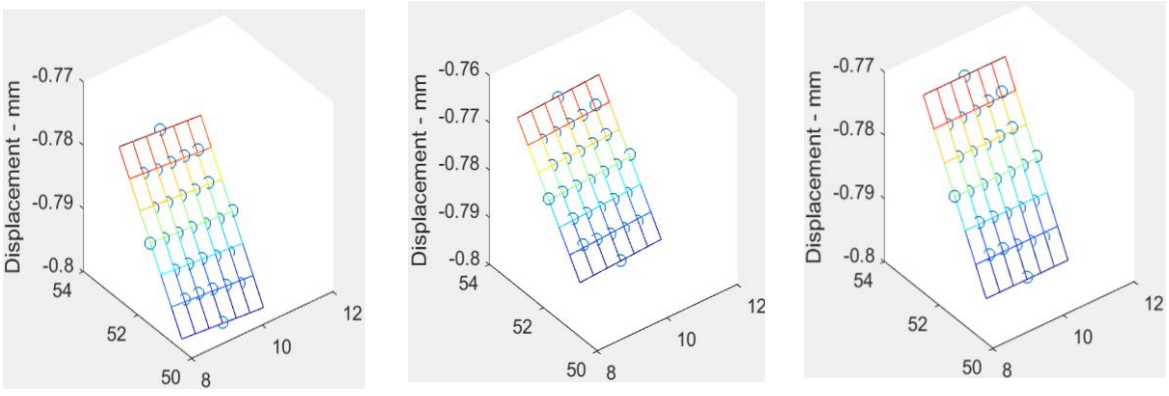

(a) *(b)* *(c)*

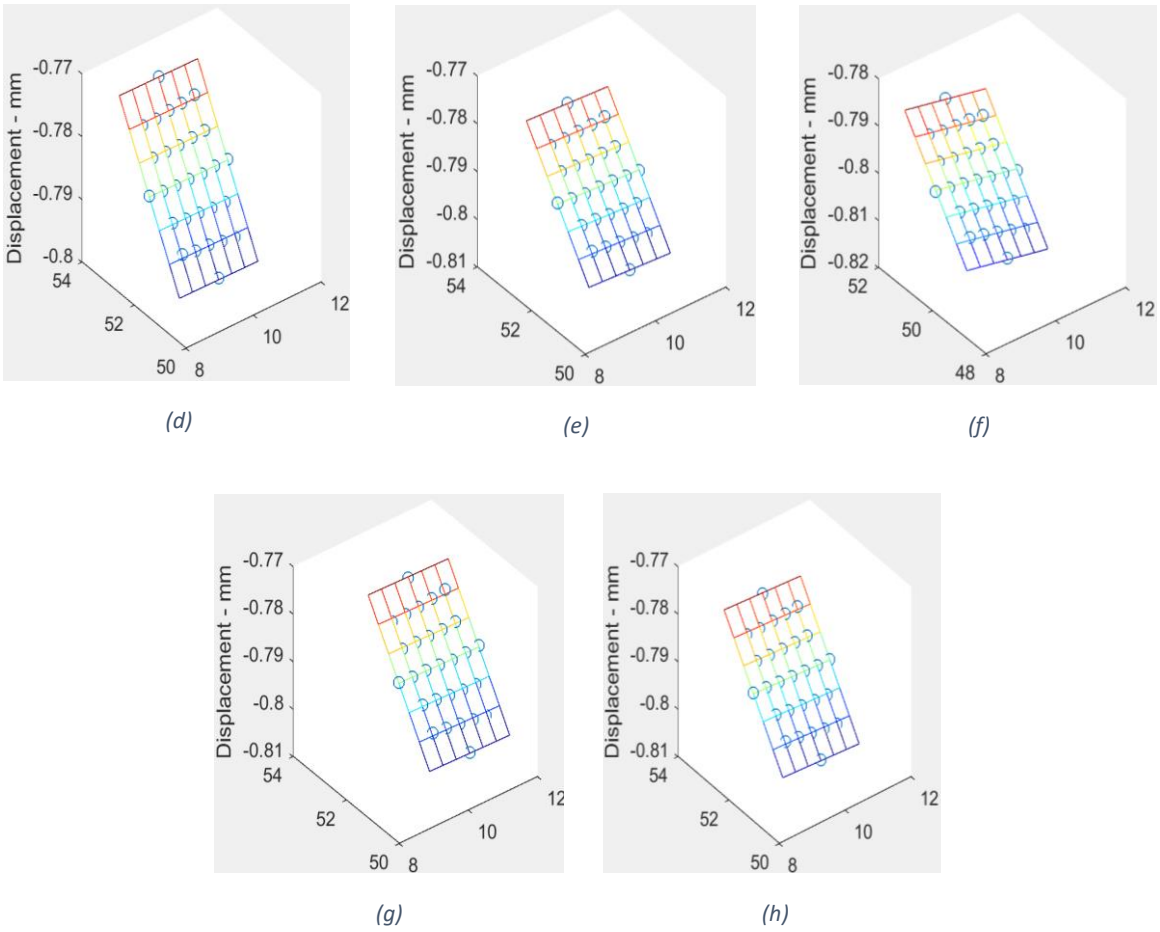

Figure 28: (a) Subset radius 10 v displacement plane. (b) Subset radius 12 v displacement plane. (c) Subset radius 14 v displacement plane. (d) Subset radius 16 v displacement plane. (e) Subset radius of 18 v displacement plane. (f) Subset radius 20 v displacement plane. (g) Subset radius 22 v displacement plane. (h) Subset radius 24 v displacement plane.

The subset radius did not appear to have the same effect on the plane applied to the v displacement data as the plane applied to the u displacement data. This was likely due to the nature of the test. Because this was a tensile test, most of the displacement was in the direction of the y axis. Because not much displacement occurred in the direction of the x axis, the u displacement values were noticeably smaller. This made the measurements more susceptible to noise. Changing the subset radius appeared to decrease the noise level in the u displacement data.

3.3.5 Exx Strain Plots

Figures 29(a) through 29(h), located on the next page, show how a change in the subset radius affected the Exx strain calculations. The images are arranged by an increasing subset radius. The subset radius values that were tested were 10, 12, 14, 16, 18, 20, 22, and 24.

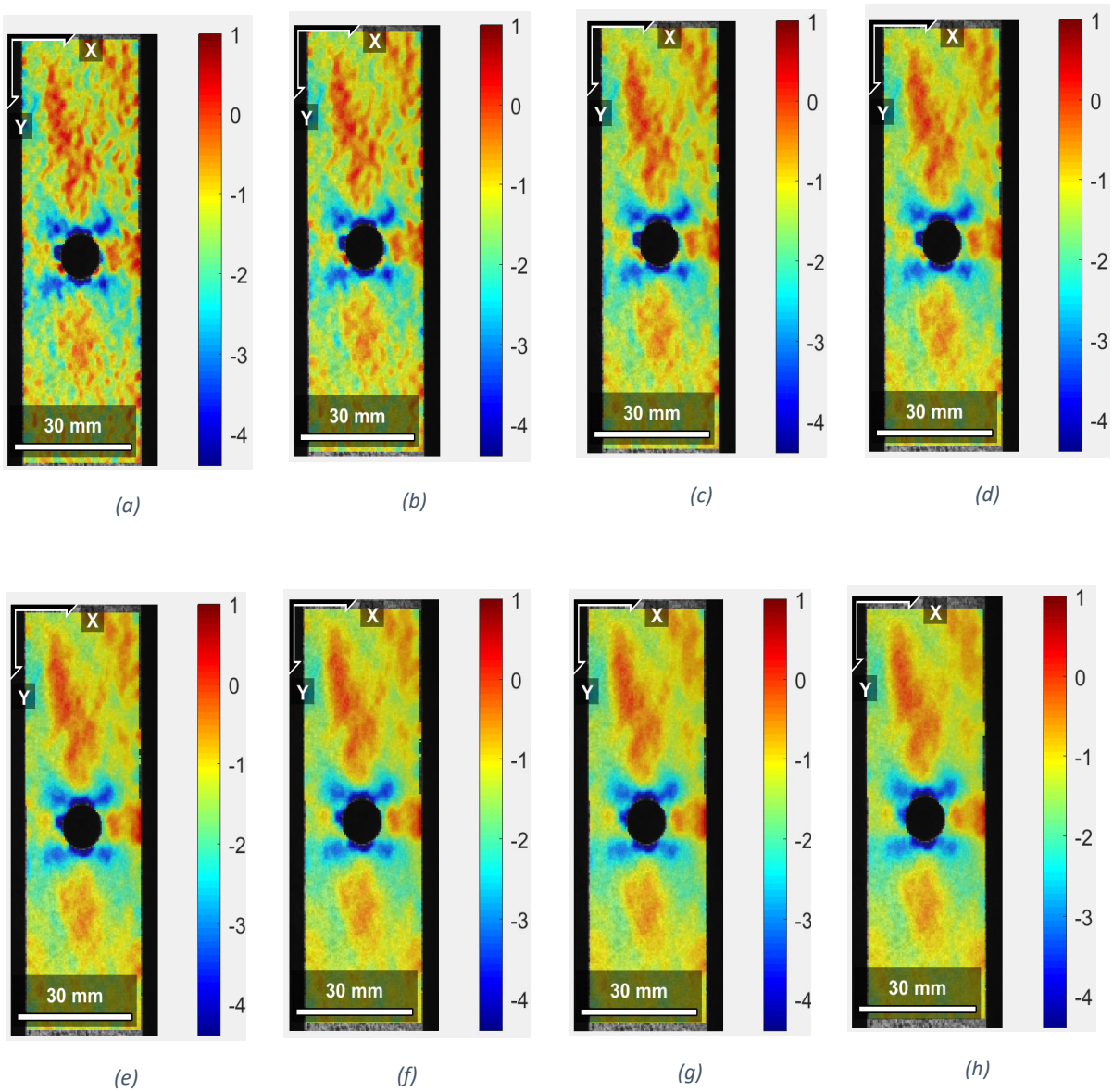

Figure 29: (a) Subset radius 10 Exx strain. (b) Subset radius 12 Exx Strain. (c) Subset radius 14 Exx strain. (d) Subset radius 16 Exx strain. (e) Subset radius of 18 Exx strain. (f) Subset radius 20 Exx strain. (g) Subset radius 22 Exx strain. (h) Subset radius 24 Exx strain.

The subset radius did affect the Exx strain calculations. As the subset radius was increased between Figures 29(a)-29(h), acute regions of high strain were smoothed over. The distinct regions of the strain profile remained the same, but there appeared to be a loss in precision with a larger subset radius.

3.3.6 Exy Strain Plots

Figures 30(a)-30(h), located on the next page, show how a change in the subset radius affected the Exy strain calculations. The images are arranged by an increasing subset radius. The subset radius values that were tested were 10, 12, 14, 16, 18, 20, 22, and 24.

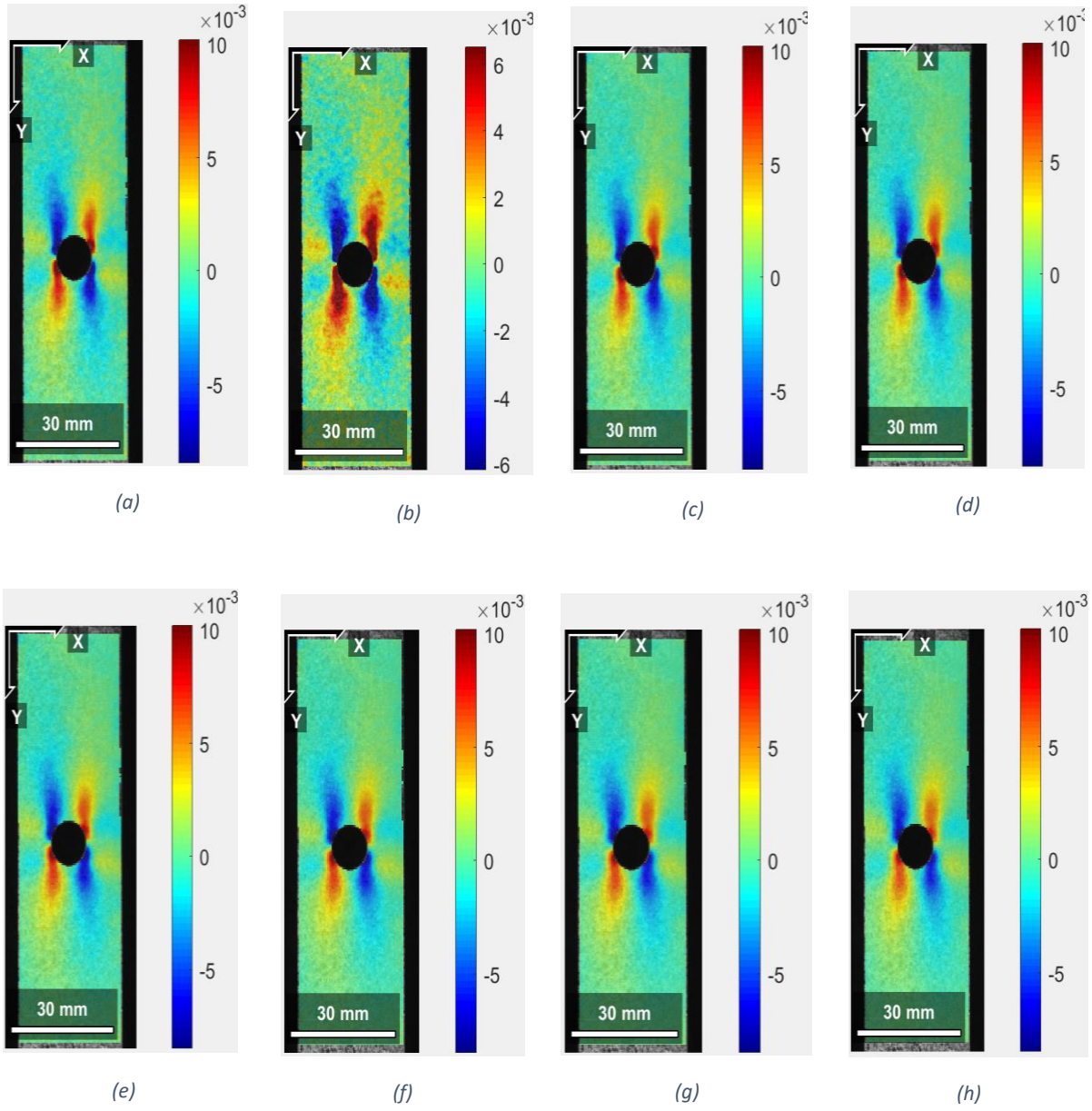

Figure 30: (a) Subset radius 10 Exy strain. (b) Subset radius 12 Exy Strain. (c) Subset radius 14 Exy strain. (d) Subset radius 16 Exy strain. (e) Subset radius of 18 Exy strain. (f) Subset radius 20 Exy strain. (g) Subset radius 22 Exy strain. (h) Subset radius 24 Exy strain.

The Exy plots showed a similar trend to the Exx strain plots. The shape and intensity of the regions of strain appear to be the same as the subset radius increased. However, small, acute regions of strain appeared to be smooth over as the subset radius increased.

3.3.7 Eyy Strain Plots

Figures 31(a)-31(h), located below, show how a change in the subset radius affected the Eyy strain calculations. The images are arranged by an increasing subset radius. The subset radius values that were tested were 10, 12, 14, 16, 18, 20, 22, and 24.

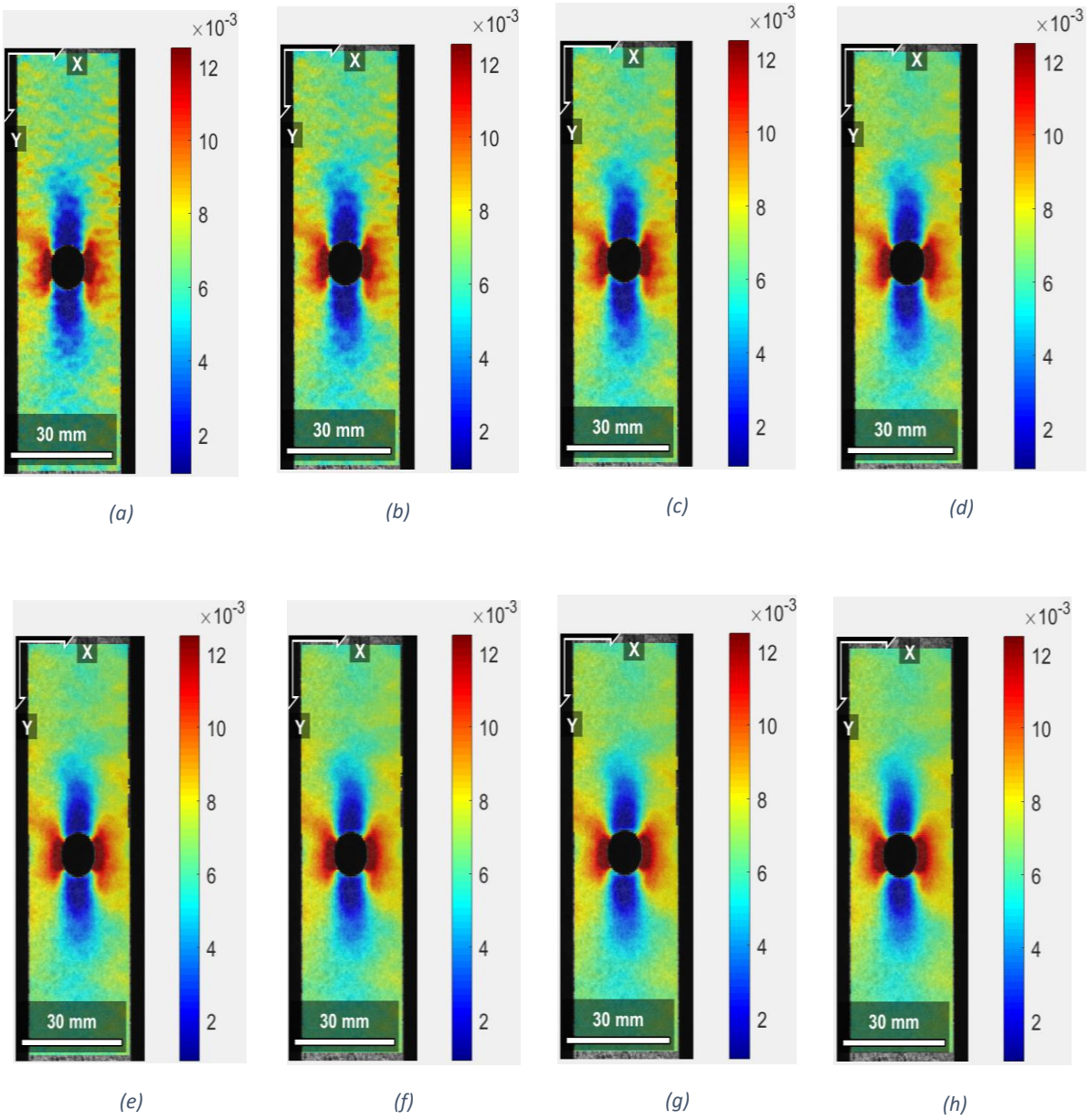

Figure 31: (a) Subset radius 10 Eyy strain. (b) Subset radius 12 Eyy Strain. (c) Subset radius 14 Eyy strain. (d) Subset radius 16 Eyy strain. (e) Subset radius of 18 Eyy strain. (f) Subset radius 20 Eyy strain. (g) Subset radius 22 Eyy strain. (h) Subset radius 24 Eyy strain.

The trends for the Eyy strain plots were the same as those for both the Exx strain plots and the Exy strain plots. A larger subset radius decreased the precision of the results and smoothed over the data.

3.3.8 Analysis

The subset radius did influence the calculations. The effects appeared to be present only in the strain calculations. Small errors were likely present in the displacement data. Due to approximating the derivative with a plane, the errors were noticeably increased in the strain data. The plots for the strain looked mostly the same as the subset radius increased, but precision appeared to go down. Regions of acute strain were smoothed over to become more homogeneous. This was especially noticeable in the Exx strain plots (Figures 30(a) through 30(h)) and the Eyy strain plots (Figures 31(a) through 31(h)).

Upon doing further research, it was found that there is a trade-off between large and small subset radius. A small subset radius has a disadvantage in that it contains fewer points. Therefore, if there is an outlier or a large quantity of noise, the calculations are affected. Additionally, it can be challenging for the DIC algorithm to differentiate one point from another as small subset may not contain enough information. However, a small subset does have an advantage in that it is able to have more precision. The DIC algorithm involves approximating displacement from a first-order differential equation. A smaller subset size can give a better approximation. In contrast, a large subset radius loses precision and has a smoothing effect on the computed values. However, the loss of precision makes a large subset size less susceptible to the effects of noisy data. Large subset sizes also have the advantage of having more data; therefore, it is more difficult for the algorithm to confuse one point with another point. (Pan et al., 2009)

A subset radius of 20 was chosen for the optimum parameter analysis. It was decided that it was unnecessary to know the exact values of acute areas of strain. What was important was that the shape and intensity of the strain regions was similar between the plots. This indicate that the overall results did not change substantially with the size of the subset radius. Additionally, a larger subset size would reduce the amount of noise in the analysis. While the noise did not appear to affect the computation substantially for the Ncorr sample images, there is a potential that other samples could be greatly affected by the noise. This is especially a concern since the images being analyzed in the optimum parameter analysis are ultrasound images as opposed to images from a more traditional camera.

3.4 Effect of Strain Radius

Figures 32(a) through 32(c), 33(a) through 33(c) and 34(a) through 34(c), located on the next two pages, show the results of the strain radius test. Each row of plots corresponds to a different type of strain. The rows correspond to Exx strain, Exy strain and Eyy strain. Each row arranges the images in order of increasing strain radius: The subset spacings that were tested include 3, 30, and 50.

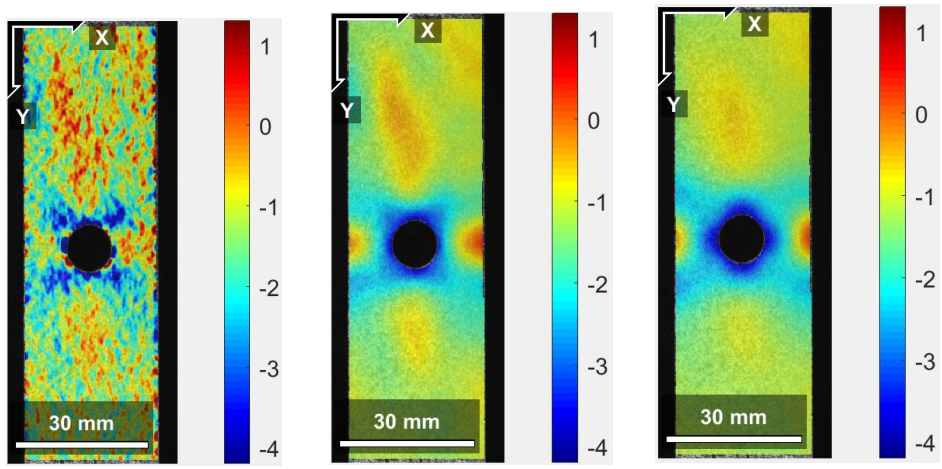

(a) *(b)* *(c)*

Figure 32: (a) The effect of a strain radius of 3 on Exx strain. (b) The effect of a strain radius of 30 on Exx strain. (c) The effect of a strain radius of 50 on Exx strain.

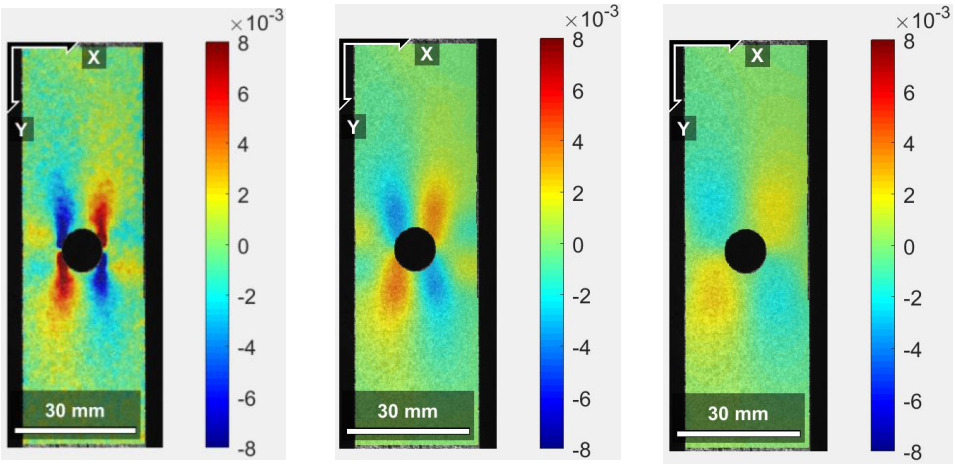

(a) *(b)* *(c)*

Figure 33: (a) The effect of a strain radius of 3 on Exy strain. (b) The effect of a strain radius of 30 on Exy strain. (c) The effect of a strain radius of 50 on Exy strain.

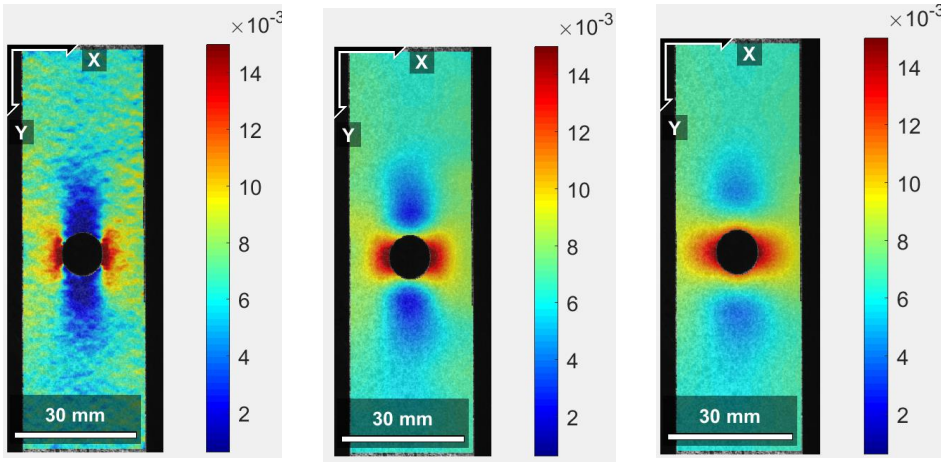

(a) *(b)* *(c)*

Figure 34: (a) The effect of a strain radius of 3 on Eyy strain. (b) The effect of a strain radius of 30 on Eyy strain. (c) The effect of a strain radius of 50 on Eyy strain.

The strain radius had a noticeable impact on the strain plots. Both the intensity and the shape of the strain profiles changed noticeably. Depending on the plot, the strain magnitude either increased or decreased. For the Exx plots, most of the positive regions of strain were eliminated as the strain radius increased. For the Exy plots, the magnitude of the positive and negative regions of strain were both reduced, and the areas containing the positive and negative regions of strain increased. For the Eyy strain, the area of the image with a large strain increased, and the area with a smaller strain decreased. Additionally, the magnitude of the lower strain regions increased.

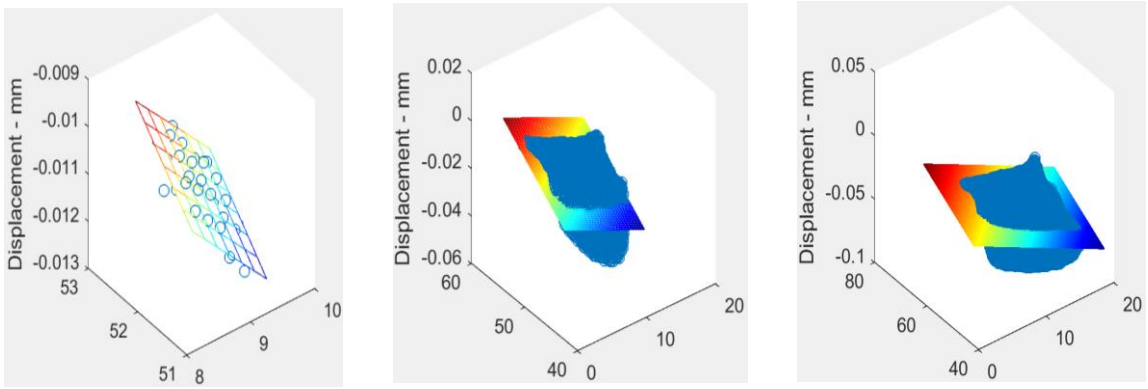

(a) *(b)* *(c)*

Figure 35: (a) The effect of a strain radius of 3 on the u displacement plane. (b) The effect of a strain radius of 30 on the u displacement plane. (c) The effect of a strain radius of 50 on the u displacement plane.

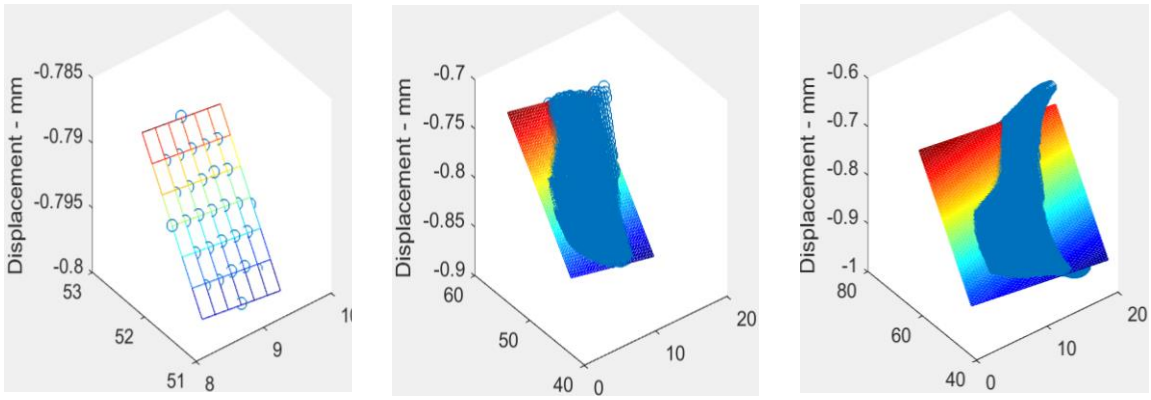

(a) *(b)* *(c)*

Figure 36: (a) The effect of a strain radius of 3 on the v displacement plane. (b) The effect of a strain radius of 30 on the v displacement plane. (c) The effect of a strain radius of 50 on the v displacement plane.

The changes between the strain plots on the previous two pages could be explained by the fit of the strain plane. As the strain radius increased, the fit for the plane became worse. This can be seen by looking at the effects of a larger strain radius on the u displacement plane (Figures 35(a) through 35(c)) and the effects of a larger strain radius on the v displacement plane (Figures 36(a) through 36(c)). As the strain calculations are determined by the fit of the plane, it made sense that the strain radius affected the accuracy of the strain calculations.

Because the strain radius had a significant impact on the accuracy of the results, it was decided that a small strain radius value was necessary. Figures 35(a) and 36(a) showed that a strain radius of 3 provided a good fit for both the u displacement plane and the v displacement plane. Most of the points are flush against the surfaces of the planes Therefore, it was determined that a strain radius of 3 would give accurate results for the optimum parameter analysis.

3.5 Effect of Strain Window Placement

Figures 37(a) through 37(c), 38(a) through 38(c), and 39(a) through 39(c) located on the next two pages, show the results of the strain window placement test. Each row of plots corresponds to a different type of strain. The rows correspond to Exx strain, Exy strain and Eyy strain. Each row shows the results from all three strain window placements for each type of strain.

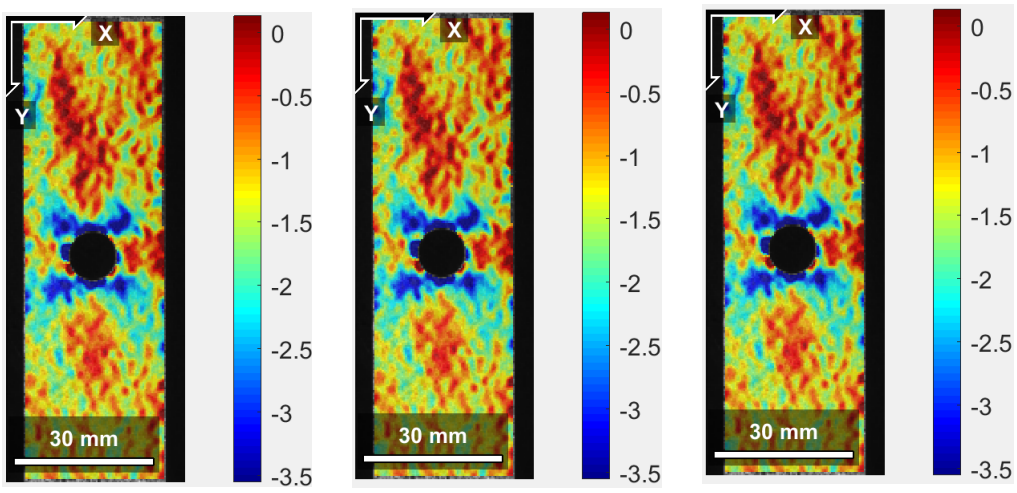

(a) *(b)* *(c)*

Figure 37: (a) The effect of the first strain window placement on Exx strain. (b) The effect of the second strain window placement on Exx strain. (c) The effect of the third strain window placement on Exx strain.

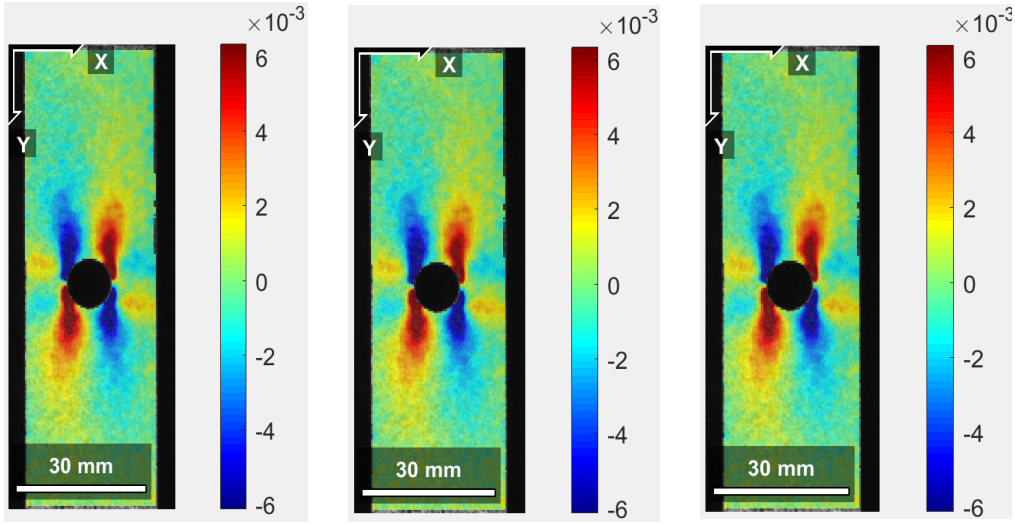

(a) *(b)* *(c)*

Figure 38: (a) The effect of the first strain window placement on Exy strain. (b) The effect of the second strain window placement on Exy strain. (c) The effect of the third strain window placement on Exy strain.

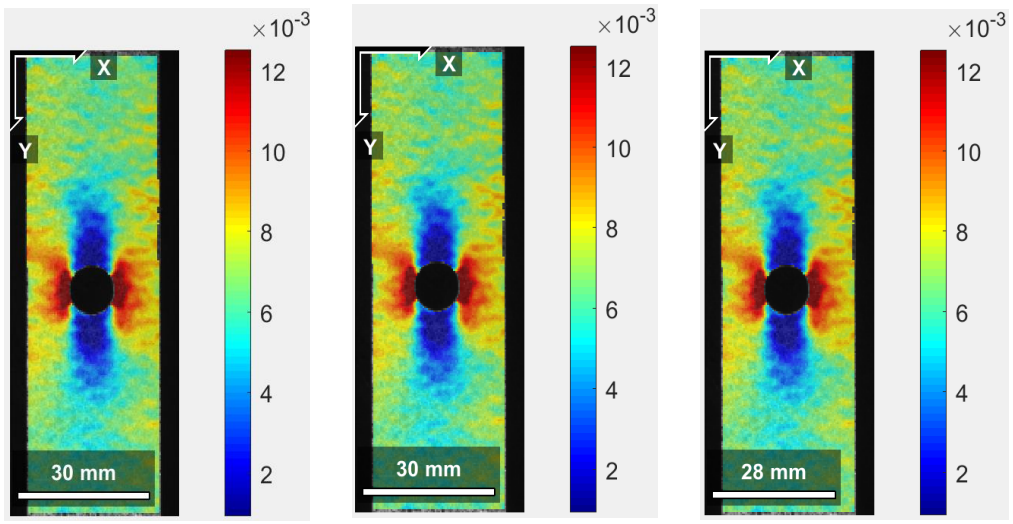

(a) *(b)* *(c)*

Figure 39: (a) The effect of the first strain window placement on Eyy strain. (b) The effect of the second strain window placement on Eyy strain. (c) The effect of the third strain window placement on Eyy strain.

The placement of the strain window had no apparent effect on the strain calculation. As the fit of the plane is important for getting accurate strain measurements, the result was surprising. The unexpected result likely stemmed from a fundamental misunderstanding of the strain window. It was assumed that the placement of the strain window functioned similarly to the placement of the initial seed. However, this result implied that the initial plane did not function as a guess from which all the strain values were calculated.

3.6 High Strain Analysis

3.6.1 Validation Test

Figures 40(a), 40(b), 41(a), 41(b), 42(a) and 42(b) located on the next two pages, show the results of the high strain analysis validation test. Each row corresponds to a different type of strain measurement. The results of the high strain analysis and normal analysis are located in the left and right columns of each row respectively.

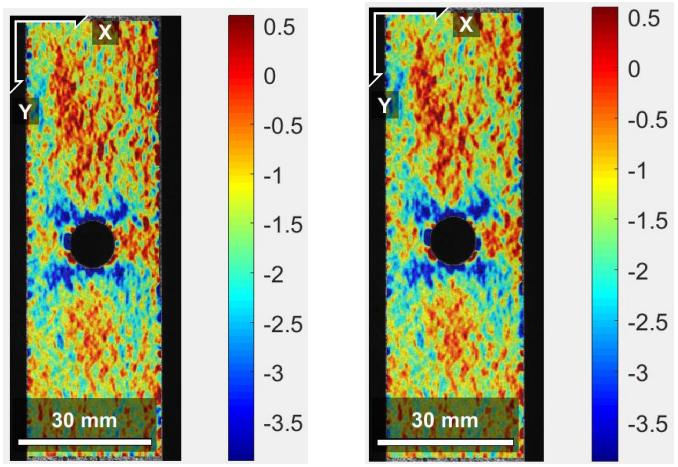

(a) *(b)*

Figure 40: (a) Exx strain from the high strain analysis. (b) Exx strain from the normal analysis.

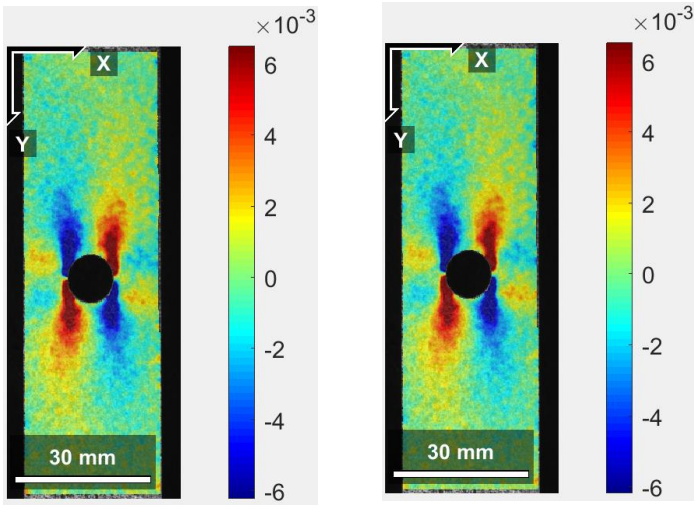

(a) *(b)*

Figure 41: (a) Exy strain from the high strain analysis. (b) Exy strain from the normal analysis.

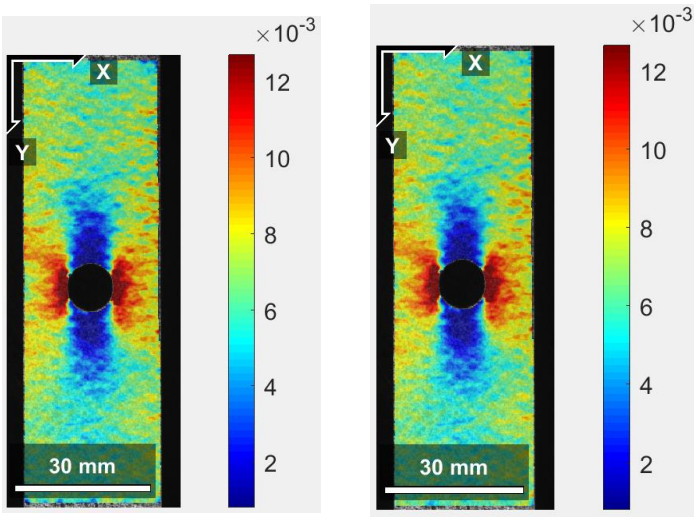

(a) *(b)*

Figure 42: (a) Eyy strain from the high strain analysis. (b) Eyy strain from the normal analysis.

It was found that the high strain analysis provided the same results for Sample 12 as the normal analysis did. This demonstrated that the high strain analysis method provides valid results. As mentioned in the methodology section, Auto-propagation and Leapfrog were both used. The combination of the settings forced Ncorr to automatically make a new guess every five images. The results of this study indicated that repeatedly changing the initial guess did not affect the validity of the analysis.

3.6.2 Normal Analysis on High Strain Image

Problems arose when Sample Image 13 was analyzed without the High Strain Analysis feature. Each subsequent image took longer to analyze than the previous image. This was especially noticeable for the initial images; however, the time increased by a smaller magnitude for later images. The analysis was not completed because the analysis times were averaging around 6-7 minutes image for the later images. With normal images, the analysis time was well under a minute. The time output for the analysis is shown by Figure 43 located below.

Figure 43: Iteration times for High Strain Image with Normal Analysis

It is important to emphasize here that this analysis was not run to completion. It is possible that the analysis would have eventually completed. However, it is not pragmatic to run a DIC analysis in which takes 6-7 minutes to analyze each image.

3.6.3 High Strain Analysis on High Strain Image

Unfortunately, the high strain analysis for the sample high strain images was unable to be completed. Multiple different high strain analysis settings were used: This included both the "Seed Propagation" setting and the "Leapfrog" setting. As mentioned earlier, Ncorr can split an ROI into multiple distinct regions with each having its own distinct initial guess. The solution to analyzing high strain images likely lies with dividing the ROI; however, this analysis requires multiple CPU cores. (Blaber et al., 2017) When installing Ncorr with the current compiler, Ncorr was unable to recognize multiple CPU cores. The issue could potentially lie with the compiler, but more research needs to be done.

3.7 Effect of ROI on Ultrasound Image Analysis

Figures 44(a) through 44(d), 45(a) through 45(d) and 46(a) through 46(d), located below and on the next page, show the results of the different ROIs on the strain calculations. Each row corresponds to a different type of strain measurement. The images in each row are ordered by the ROI number.

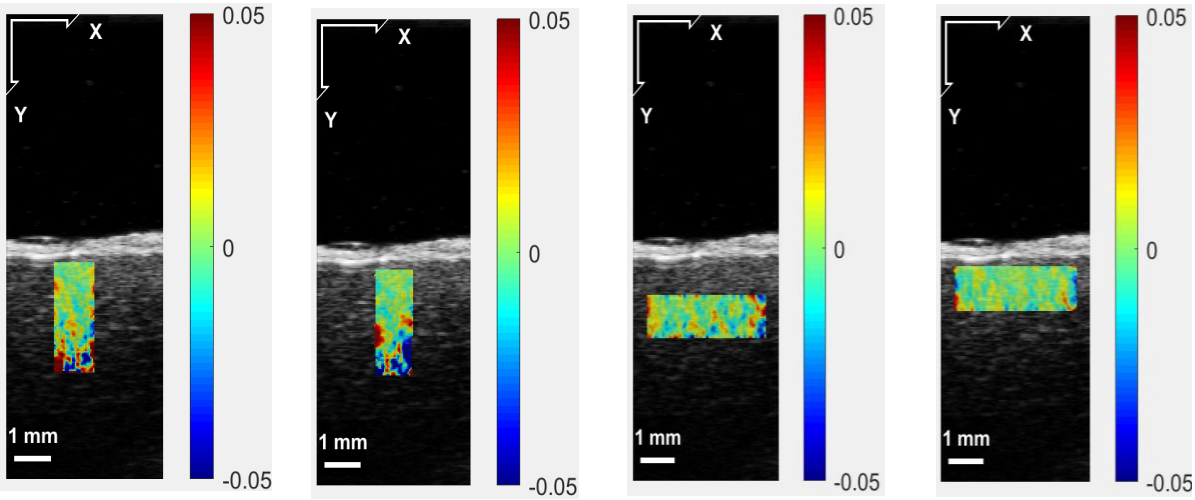

Figure 44: (a) The effect of ROI 1 on Exx strain. (b) The effect of ROI 2 on Exx strain. (c) The effect of ROI 3 on Exx strain. (d) The effect of ROI 4 on Exx strain.

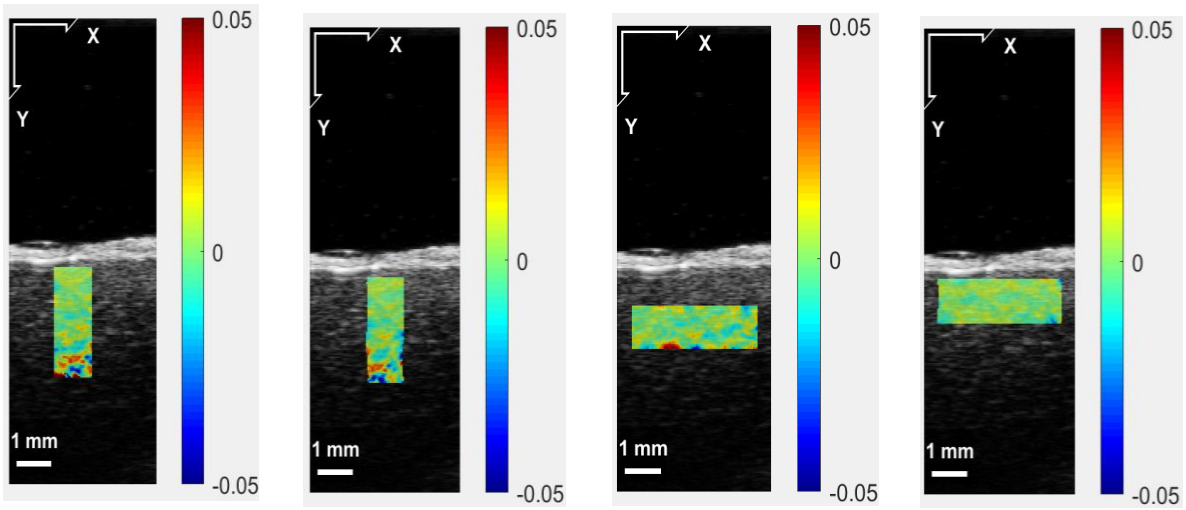

(a) *(b)* *(c)* *(d)*

Figure 45: (a) The effect of ROI 1 on Exy strain. (b) The effect of ROI 2 on Exy strain. (c) The effect of ROI 3 on Exy strain. (d) The effect of ROI 4 on Exy strain.

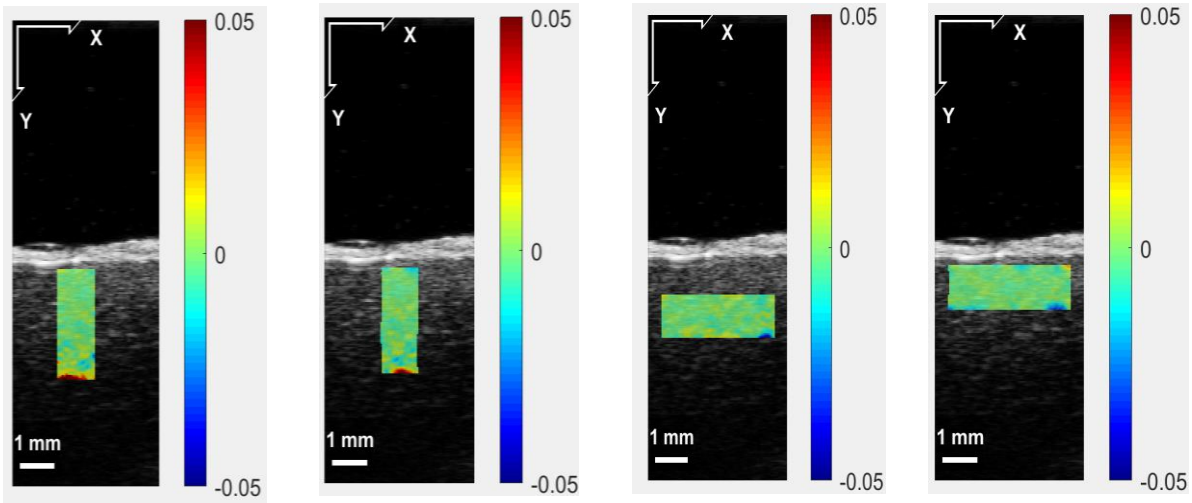

(a) *(b)* *(c)* *(d)*

Figure 46: (a) The effect of ROI 1 on Eyy strain. (b) The effect of ROI 2 on Eyy strain. (c) The effect of ROI 3 on Eyy strain. (d) The effect of ROI 4 on Eyy strain.

Figures 47(a) through 47(d) and 48(a) through 48(d), located on the next page, show the results of the different ROIs on the fit of the u displacement and v displacement planes. Figures 47(a) through 47(d) correspond to the u displacement planes and Figures 48(a) through 48(d) correspond to the v displacement planes. The figures in each row are ordered by the ROI number.

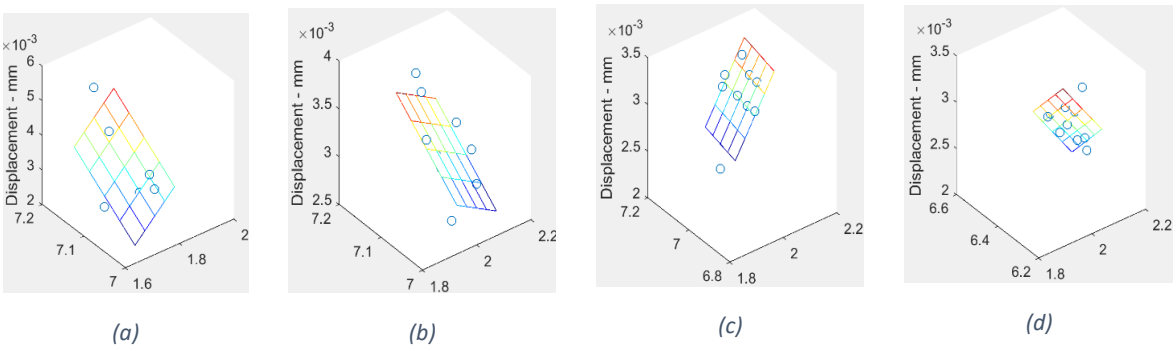

Figure 47: (a) The effect of ROI 1 on the u displacement plane. (b) The effect of ROI 2 on the u displacement plane. (c) The effect of ROI 3 on the u displacement plane. (d) The effect of ROI 4 on the u displacement plane.

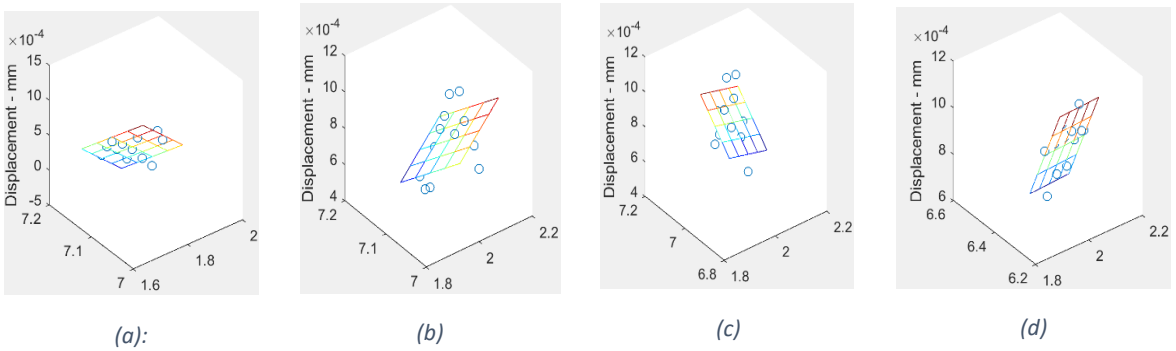

Figure 48: (a) The effect of ROI 1 on the v displacement plane. (b) The effect of ROI 2 on the v displacement plane. (c) The effect of ROI 3 on the v displacement plane. (d) The effect of ROI 4 on the v displacement plane.

The shape and placement of the ROI had a noticeable impact on noise in the data. Additionally, there appeared to be no correlation between the noise for the u-displacement plane and the v-displacement plane. As the strain calculations were based on both the u-displacement and the v-displacement, it was difficult to determine the best ROI without a way of quantifying the fit of the planes. From the result, a conclusion was made that the ROI placement and shape affected the strain calculation, but more information was needed to draw further conclusions. ROI 2, represented by Figures 44(b), 45(b), and 46(b), was ultimately chosen for further analysis as it was in the center of the image showed displacement and strain at varying depths. The variation in depth is important because the displacement of brain tissue can vary in depth. This is partly due to the bridging veins restricting motion of the brain in certain areas (Hardy et al, 2017). As the displacement varies, there is likely to be variations in the strain of the brain tissue. Higher regions of strain are more likely to cause an injury of the brain tissue. If only one specific depth of the brain tissue were being analyzed, important information on the displacement and strain could be missed.

3.8 Optimum Parameter Analysis

Figures 49(a), 49(b), 50(a) and 50(b), located below, show plots of both u-displacement and Exx strain at both the initial image and at the image with the maximum displacement and strain. The initial image is shown in the let column of each row, and the maximum value plot is shown in the right column of each row.

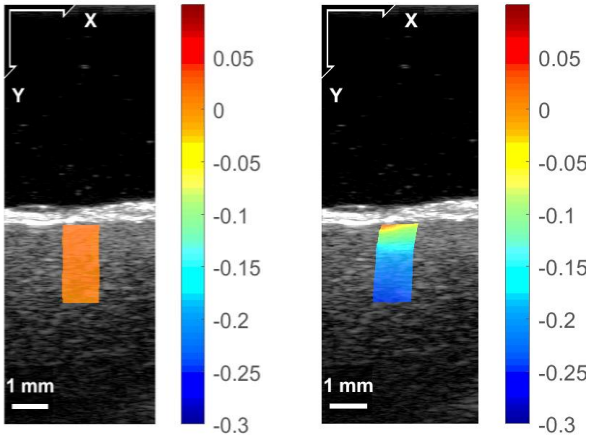

(a) *(b)*

Figure 49: (a) Initial displacement plot for ultrasound images. (b) Maximum displacement plot for ultrasound images.

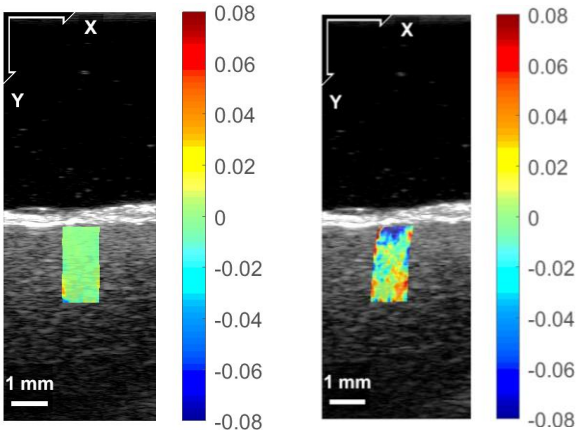

(a) *(b)*

Figure 50: (a) Initial strain plot for ultrasound images. (b) Maximum strain plot for ultrasound images.

For both Figure 49(a) and Figure 50(a), the color of the plot is uniform, indicating that both the strain and displacement of the points are zero. For Figure 49(b) and Figure 50(b), the shear deformation of the ROI relative to the dura mater was apparent. Also, Figure 49(b), the maximum displacement plot, gave a clear relationship between the displacement from the dura and the magnitude of the displacement: As the displacement from the dura increased, magnitude of the u-displacement also increased. Unfortunately, there were no clear conclusions that could be drawn from Figure 50(b) which

is the maximum Exx strain plot. The plot had an unclear pattern of both positive and negative strain regions. It was hypothesized that noise was contributing to the abnormal strain pattern. The primary reason for this was that the planes fitted to the displacement data were used to approximate partial derivatives. The partial derivate approximations amplified any noise that was in the displacement data. Research has shown, that speckle patterns contribute to the noise from a DIC analysis. As speckle patterns are a common source of noise in ultrasound images, the speckle pattern likely contributed to the errors in the strain calculations.

Maximum displacement values at the surface, 1mm from the surface, and 2 mm from the surface were compared between TEMA and Ncorr. It was found that at 1 mm deep and 2mm deep, there was a small percent difference between the measured displacements from Ncorr and TEMA. The percent difference measurements for 1 mm deep and 2 mm deep were found to be 2.22% and 2.24% respectively. At the surface, a much larger percent difference of 32% was calculated. It was possible that the error originated from TEMA as it was difficult to get a displacement measurement close to the surface of the brain tissue. Likewise, the error could have originated from the DIC analysis as the surface region was close to the boundary of the ROI. A table containing the measured displacement values and calculated percent differences is shown below.

Table 2: DIC Validation

Test Method	Surface	1 mm deep	2 mm deep
TEMA	0.058 mm	0.178 mm	0.226 mm
DIC	0.042 mm	0.182 mm	0.221 mm
Percent Difference	**32%**	**2.22%**	**2.24%**

The results of the DIC analysis are significant as it shows that DIC can calculate displacement values to TEMA. The large error near the surface of the brain tissue is a limitation of this study. There is no way to improve TEMA's point tracking ability near the surface of the brain tissue. Additionally, the ROI used in the DIC analysis can not be drawn any bigger as that would include the meninges in the ROI. Because the meninges would not be moving, this would likely have a noticeable impact on the DIC calculations.

3.9 Effect of Subset Radius on Noise

3.9.1 U-Displacement Planes

Figures 51(a) through 51(o), located on the next two pages, show how a change in the subset radius affects the fit of the plane applied to the u displacement data for the strain calculations performed on the ultrasound images. The images are arranged by an increasing subset radius. The subset radius values that were tested were 10, 12, 14, 16, 18, 20, 22, 24, 26, 28, 30, 32, 34, 36 and 38.

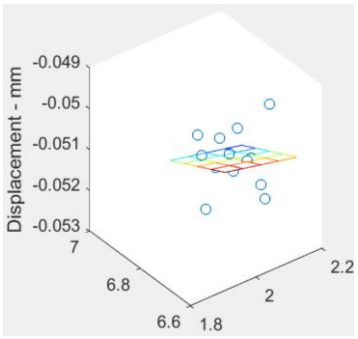
Displacement - mm
-0.049
-0.05
-0.051
-0.052
-0.053
7
6.8
6.6
1.8
2
2.2

(a)

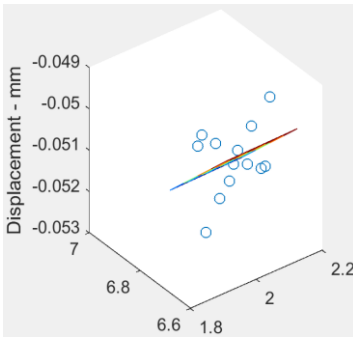
Displacement - mm
-0.049
-0.05
-0.051
-0.052
-0.053
7
6.8
6.6
1.8
2
2.2

(b)

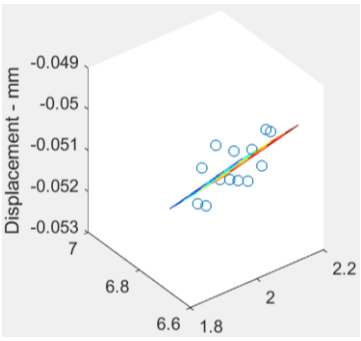
Displacement - mm
-0.049
-0.05
-0.051
-0.052
-0.053
7
6.8
6.6
1.8
2
2.2

(c)

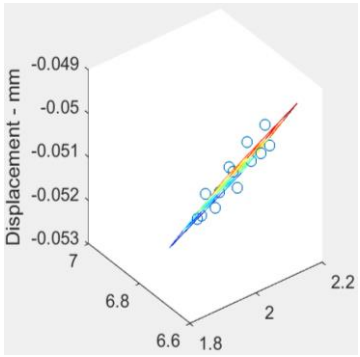
Displacement - mm
-0.049
-0.05
-0.051
-0.052
-0.053
7
6.8
6.6
1.8
2
2.2

(d)

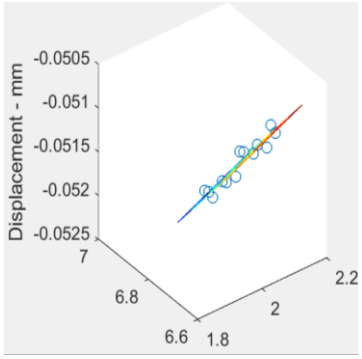
Displacement - mm
-0.0505
-0.051
-0.0515
-0.052
-0.0525
7
6.8
6.6
1.8
2
2.2

(e)

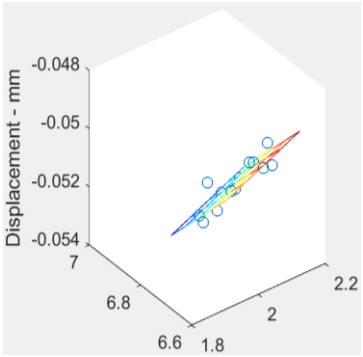
Displacement - mm
-0.048
-0.05
-0.052
-0.054
7
6.8
6.6
1.8
2
2.2

(f)

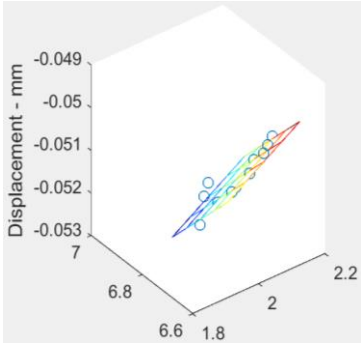
Displacement - mm
-0.049
-0.05
-0.051
-0.052
-0.053
7
6.8
6.6
1.8
2
2.2

(g)

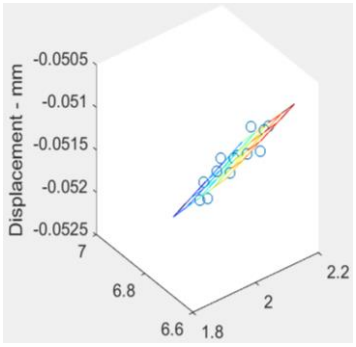
Displacement - mm
-0.0505
-0.051
-0.0515
-0.052
-0.0525
7
6.8
6.6
1.8
2
2.2

(h)

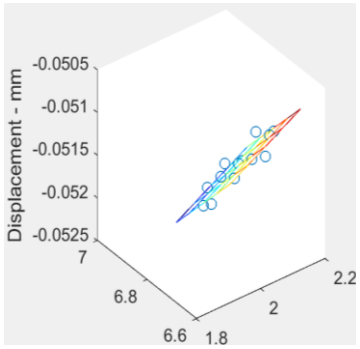
Displacement - mm
-0.0505
-0.051
-0.0515
-0.052
-0.0525
7
6.8
6.6
1.8
2
2.2

(i)

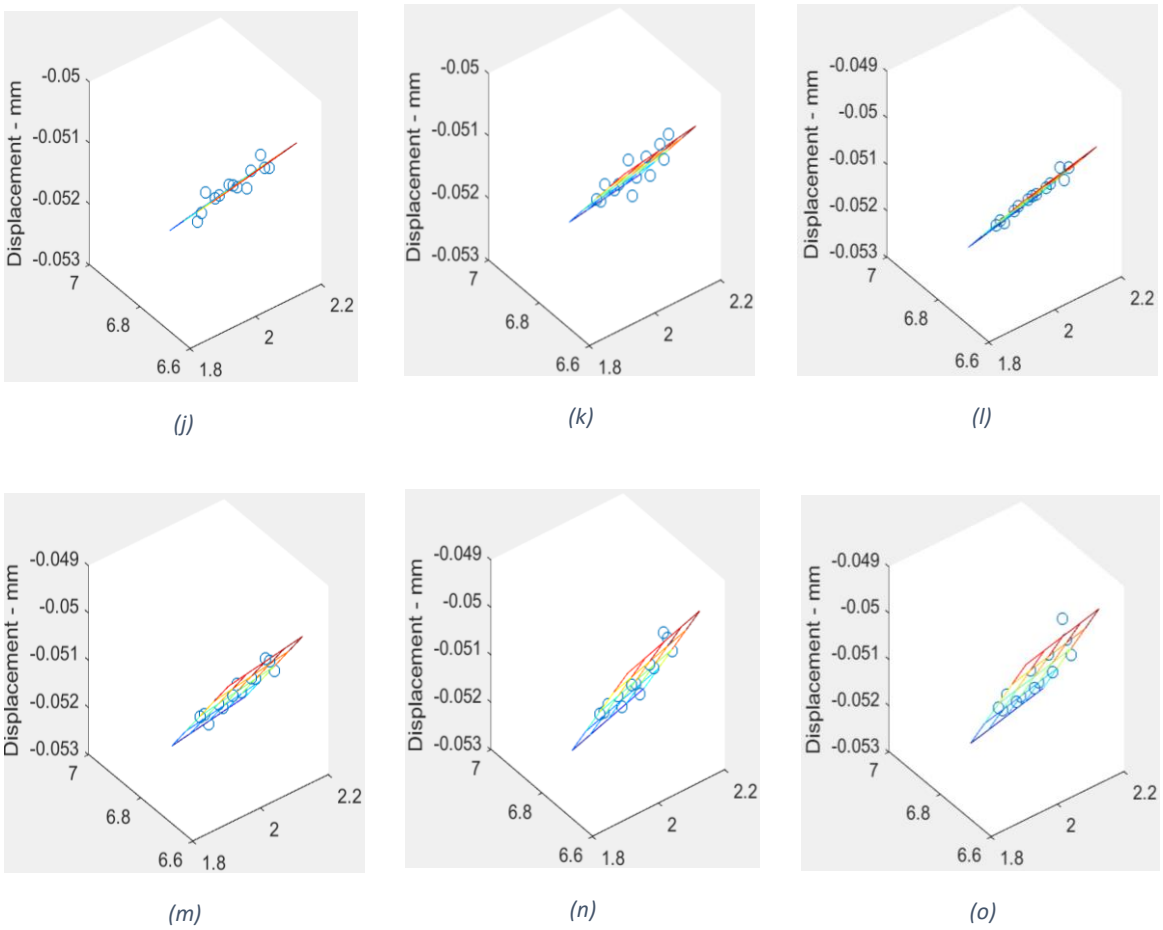

Figure 51: (a) Subset radius 10 u displacement plane. (b) Subset radius 12 u displacement plane. (c) Subset radius 14 u displacement plane. (d) Subset radius 16 u displacement plane. (e) Subset radius 18 u displacement plane. (f) Subset radius 20 u displacement plane. (g) Subset radius 22 u displacement plane. (h) Subset radius 24 u displacement plane. (i) Subset radius 26 u displacement plane. (j) Subset radius 28 u displacement plane. (k) Subset radius 30 u displacement plane. (l) Subset radius 32 u displacement plane. (m) Subset radius 34 u displacement plane. (n) Subset radius 36 u displacement plane. (o) Subset radius 38 u displacement plane.

As the subset radius was increased, the fit between the displacement data and the plane improved. The trend was especially noticeable between Figures 51(a)-51(e). By the time the strain radius reached a value of 16, a large portion of the noise had been reduced. However, increasing the subset radius past a value of 16 did appear to decrease the noise further but at a slower rate. The results supported the earlier claim that the subset radius affected the noise of the data.

3.9.2 V-Displacement Plane

Figures 52(a)-52(o), located on the next two pages, show how a change in the subset radius affects the fit of the plane applied to the v displacement data for the strain calculations performed on the ultrasound images. The images are arranged by an increasing subset radius. The subset radius values that were tested were 10, 12, 14, 16, 18, 20, 22, 24, 26, 28, 30, 32, 34, 36 and 38.

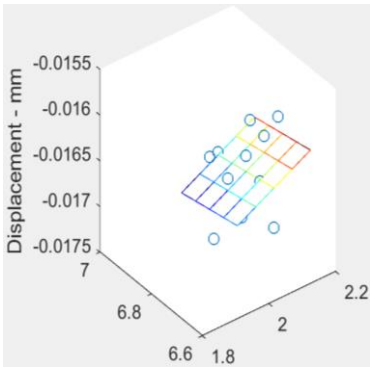
Displacement - mm
-0.0155
-0.016
-0.0165
-0.017
-0.0175
7
6.8
6.6
1.8
2
2.2

(a)

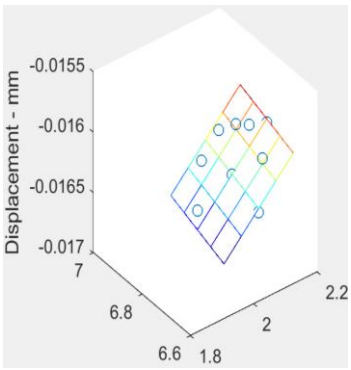
Displacement - mm
-0.0155
-0.016
-0.0165
-0.017
7
6.8
6.6
1.8
2
2.2

(b)

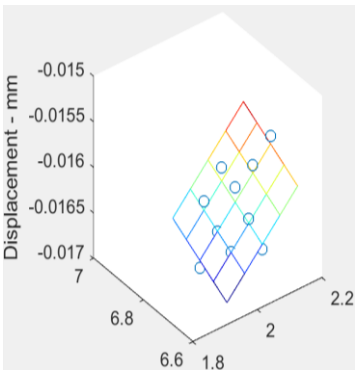
Displacement - mm
-0.015
-0.0155
-0.016
-0.0165
-0.017
7
6.8
6.6
1.8
2
2.2

(c)

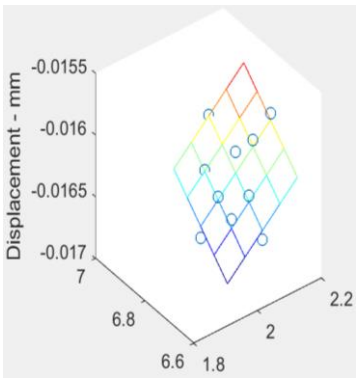
Displacement - mm
-0.0155
-0.016
-0.0165
-0.017
7
6.8
6.6
1.8
2
2.2

(d)

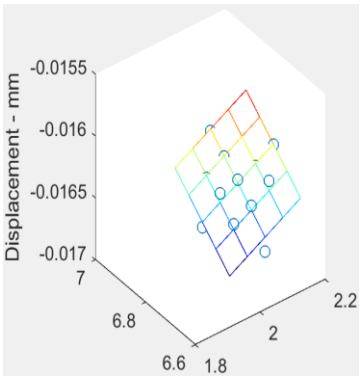
Displacement - mm
-0.0155
-0.016
-0.0165
-0.017
7
6.8
6.6
1.8
2
2.2

(e)

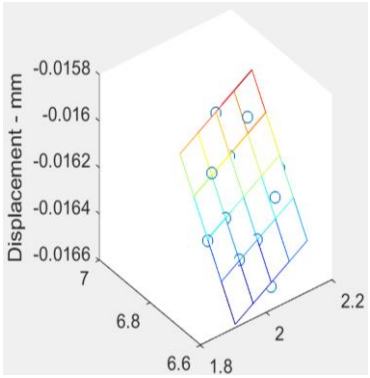
Displacement - mm
-0.0158
-0.016
-0.0162
-0.0164
-0.0166
7
6.8
6.6
1.8
2
2.2

(f)

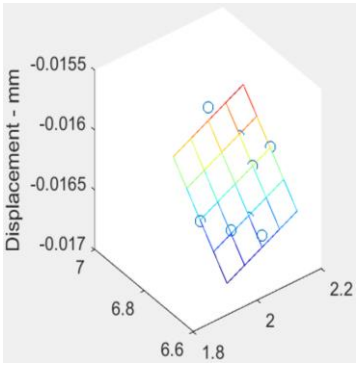
Displacement - mm
-0.0155
-0.016
-0.0165
-0.017
7
6.8
6.6
1.8
2
2.2

(g)

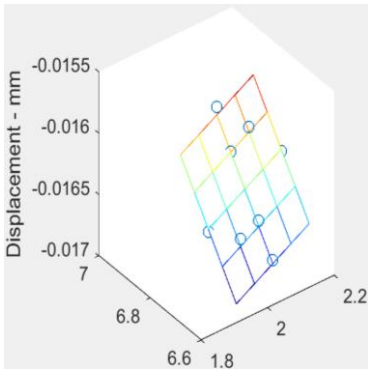
Displacement - mm
-0.0155
-0.016
-0.0165
-0.017
7
6.8
6.6
1.8
2
2.2

(h)

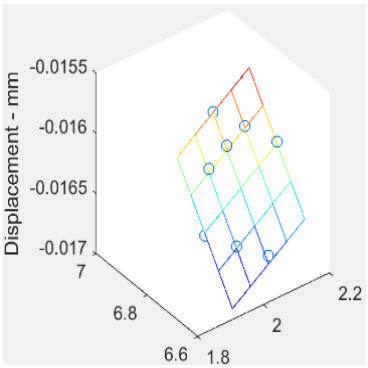
Displacement - mm
-0.0155
-0.016
-0.0165
-0.017
7
6.8
6.6
1.8
2
2.2

(i)

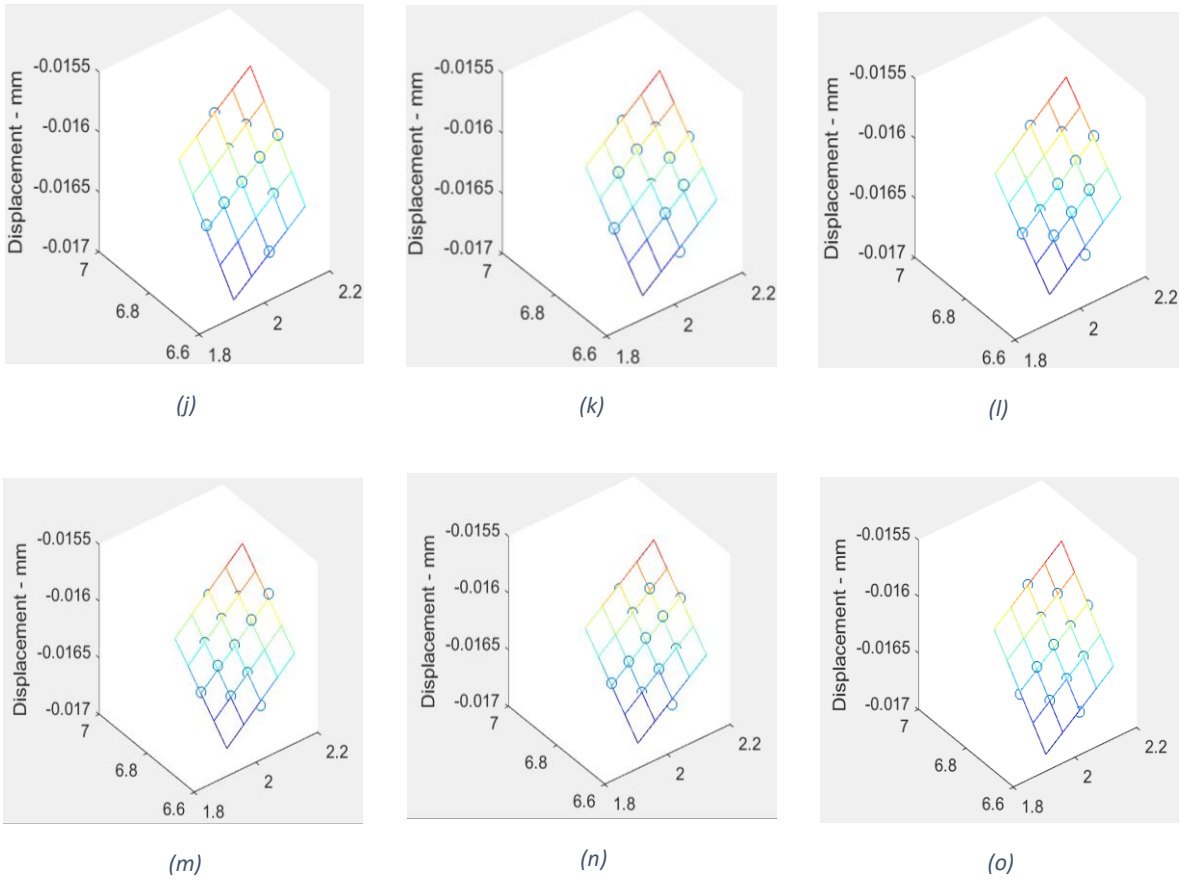

Figure 52: (a) Subset radius 10 v displacement plane. (b) Subset radius 12 v displacement plane. (c) Subset radius 14 v displacement plane. (d) Subset radius 16 v displacement plane. (e) Subset radius 18 v displacement plane. (f) Subset radius 20 v displacement plane. (g) Subset radius 22 v displacement plane. (h) Subset radius 24 v displacement plane. (i) Subset radius 26 v displacement plane. (j) Subset radius 28 v displacement plane. (k) Subset radius 30 v displacement plane. (l) Subset radius 32 v displacement plane. (m) Subset radius 34 v displacement plane. (n) Subset radius 36 v displacement plane. (o) Subset radius 38 v displacement plane.

The results were similar to the results to the plane that was fit to the u displacement data but to a lesser extent. As the subset radius was increased, the fit between the displacement data and the plane improved. However, unlike the planes fit to the u displacement data, most of the noise appeared to be reduced by a strain radius of 14. Therefore, it can be concluded that for the testing setup used in this study, u displacement is more susceptible to noise than v displacement.

3.9.3 Exx Strain Plots First Scale Bar

Figures 53(a)-53(h), located on the next page, show the effect of the subset radius on the noise for the first eight subset radius values that were tested. The images are ordered from the smallest subset radius to the largest subset radius.

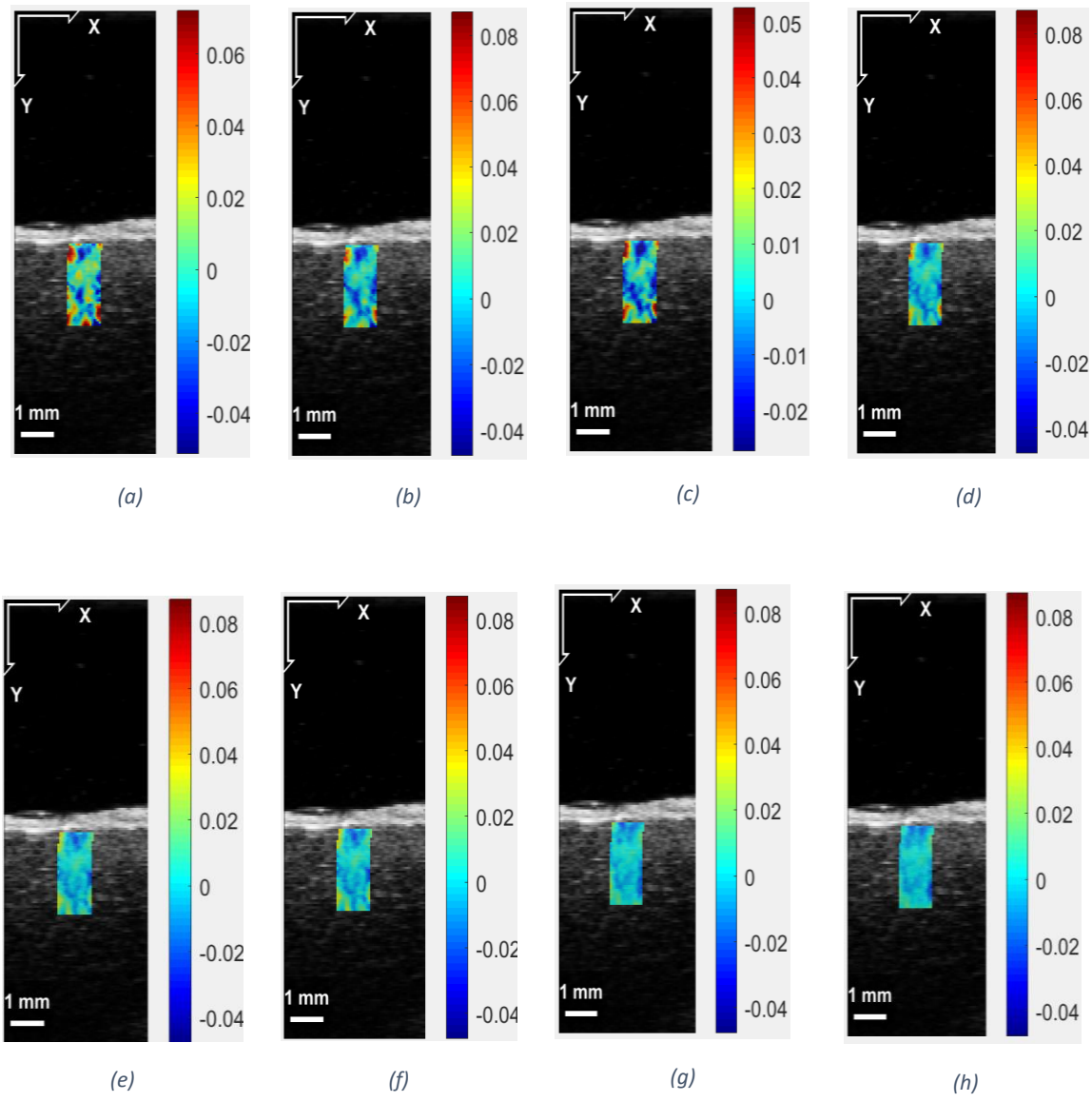

Figure 53: (a) Subset radius 10 Exx strain. (b) Subset radius 12 Exx Strain. (c) Subset radius 14 Exx strain. (d) Subset radius 16 Exx strain. (e) Subset radius of 18 Exx strain. (f) Subset radius 20 Exx strain. (g) Subset radius 22 Exx strain. (h) Subset radius 24 Exx strain.

The results were similar to the results for the planes fitted to the u displacement data. This made sense as there appeared to be more noise in the u displacement data than the v displacement data. Therefore, it would make sense that the noise pattern of the strain plots would more closely resemble the noise pattern of the planes fitted to the u displacement data. By Figure 53(e), the figures began to look similar to each other. It was determined that a smaller scalebar should be used for additional subset radius values that would be tested. This would make it possible to see if there were any remaining noise at a smaller scale.

3.9.4 Exx Strain Plots Second Scale Bar

Figures 54(a)-54(g), located below, show the effects on the Exx strain due to increasing the subset radius from 26-38. The images are arranged by the smallest to the largest subset radius. A smaller scale bar is used for these plots to see if there was any effect on the noise of the strain data at a smaller scale. 53(e)-53(h) from the previous section looked similar to each other at the scalebar used. The new scalebar was used to see if any noise was still present.

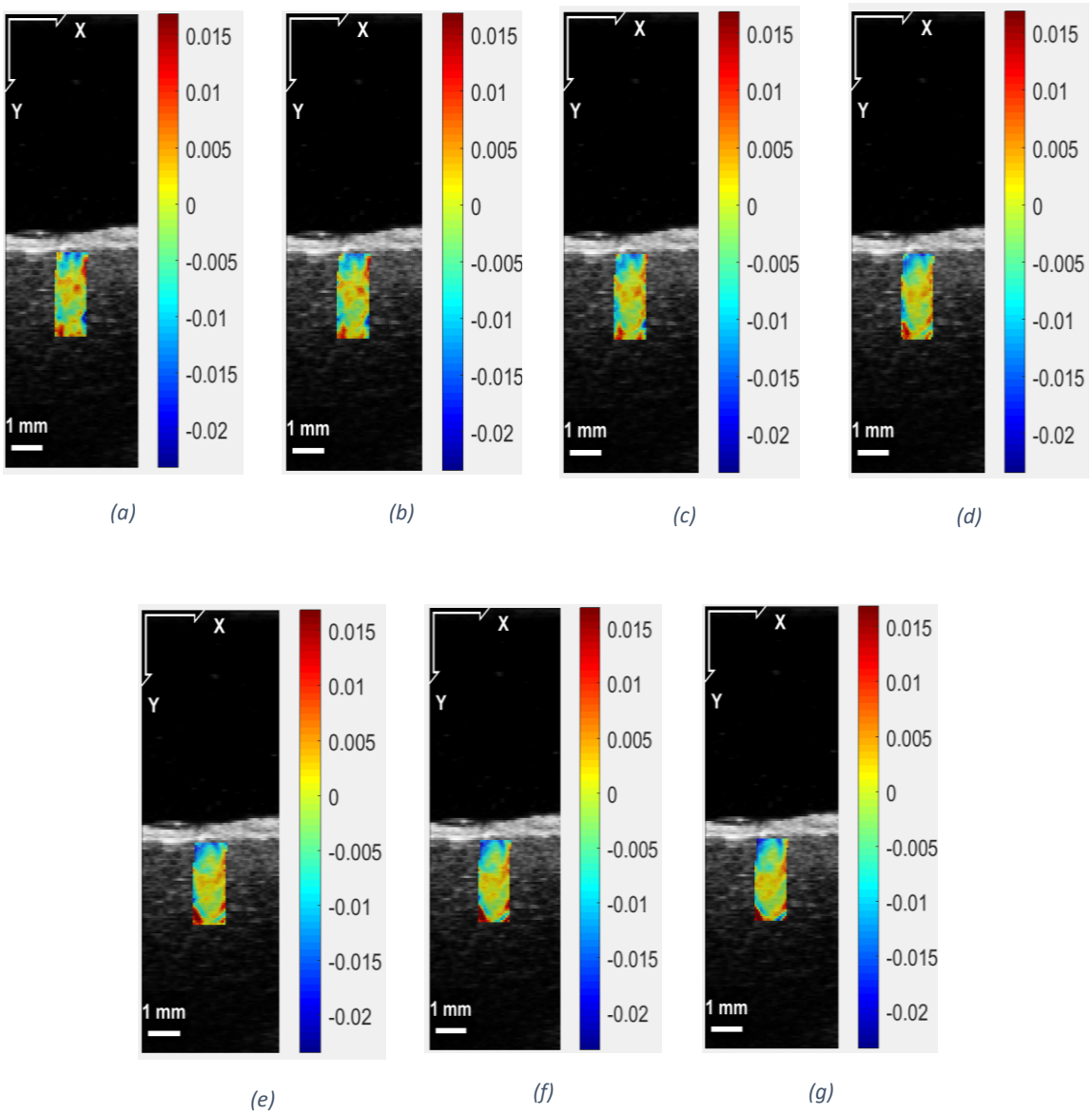

Figure 54: (a) Subset radius 26 Exx strain. (b) Subset radius 28 Exx Strain. (c) Subset radius 30 Exx strain. (d) Subset radius 32 Exx strain. (e) Subset radius of 34 Exx strain. (f) Subset radius 36 Exx strain. (g) Subset radius 38 Exx strain. (h) Subset radius 40 Exx strain.

By reducing the scalebar for Figures 54(a)-54(g), it was shown that there was still noise in the data. A subset radius of 38 was the largest subset radius that could be used without causing an error. This was likely because the size of a subset in the analysis was bigger than the ROI that was used.

3.9.5 Analysis

The results matched what was expected based on the analysis of the results from the Sample 12 subset radius test. As the subset radius was increased, the noise decreased. However, the noise did remain on a smaller scale. However, the subset radius appeared to have less of an effect on the noise at larger subset radius values. The final plots were almost indistinguishable from each other. While the reduced noise is desirable, the magnitudes of the strain values were likely affected as well. More research would have to be done to find a good balance between the reduced noise from a large subset radius and the increased precision from a small subset radius.

Chapter 4: Discussion

The main goal of this study was unsuccessful. While the DIC analysis was able to provide strain plots of the brain deformation, there was too much noise to analyze the data. Therefore, it can be concluded that the Ncorr software is unable to analyze strain from high-speed, high-frequency B-mode ultrasound images. The strain plot is shown in Figure 50(b). Preliminary attempts to reduce the noise in the strain plots were also unsuccessful. For example, when increasing the subset radius, the noise did decrease, but it was not by enough to make it possible to analyze the data. The problem is likely due to inherent noise in ultrasound images. Some scientific literature points to speckled patterns within images causing an inherent noise in DIC data. (Pan el al., 2009) Speckle-noise is a common type of noise in ultrasound images, and it effectively adds extra points and data to an ultrasound image (Kremkau et al., 1986). Research should be done to see if a Fourier transform can reduce the speckled pattern and filter out the noise from the ultrasound images. More research could also be done into the correlation coefficient values used in DIC. It is possible to eliminate points with high correlation values from the analysis. Eliminating these points could reduce the amount of random errors in the analysis.

However, while the analysis of the strain plots was unsuccessful, the analysis of the displacement plots was successful. The displacement plot data, shown by Figure 49(b), showed how displacement varies with depth in the brain tissue. This is supported by a prior study which showed that displacement in the brain tissue varies with depth (Hardy et al, 2007). Additionally, the displacement values in the brain tissue matched with similar displacement measurements from TEMA. This is shown by Table 2. Ncorr has a distinct advantage in that it can analyze the displacement of multiple points at a time and generate displacement vector fields. Therefore, Ncorr and DIC still have a potential to innovate research in Injury Biomechanics as current software, such as TEMA, only analyzes points corresponding to small number of points corresponding to fiducials.

More work still needs to be done with respect to analyzing high strain images. Primarily, work needs to be done to successfully complete an analysis with a high strain image. The key likely lies with dividing up the ROI into multiple regions. As mentioned earlier, this allows the computations of the regions to be run in parallel, and each region has its own initial guess. Unfortunately, the Ncorr files would not compile correctly if more than one CPU core was selected for the analysis. To use multiple regions, the OpenMP support is required. The compiler that was used for the study could be the source of the errors. A new MEX compiler should be used to see if the compiling process proceeds properly. If the compiler

fixes the problem, the parameter studies should be run again with the high strain images. It is likely that some of the parameters will respond differently when more movement occurs in the image. More work can also still be done in researching the DIC parameters. This study also gave useful insights into the subset spacing, strain radius, and subset radius. However, much more can be learned about the impact of the initial guess, the correlation coefficients, the ROI placement and shape and the strain window. Perhaps, learning more about these other DIC parameters could help with analyzing the high strain images.

A way also needs to also be found to quantify the fit of the plane with respect to the displacement and coordinate values. This is especially apparent in the ROI placement study. There is a limit to how much the planes can be interpreted based on qualitative information alone. The plane coefficients were not found in the output from Ncorr. If the plane coefficients could be determined, a fit could be found based on the normal vector of the plane and the points being fitted to the plane. The solution to this problem could involve either modifying Ncorr's code to display the plane coefficients in the MATLAB command window. Additionally, the plane coefficients could be calculated because the strain values are known. Perhaps, if a way is found to quantify the fit, the fit can better be related to the amount of noise in the strain data.

Chapter 5: Conclusions

- 2D DIC was unable to accurately analyze strain of PMHS brain tissue from high-speed, high-frequency B-mode ultrasound images
- 2D DIC accurately computed displacement of PMHS brain tissue with results comparable to TEMA except at the surface of the brain tissue
- Speckle-noise patterns should be considered when analyzing high-speed, high-frequency B-mode ultrasound images
- Quantifying the fit of the strain plane could make it easier to analyze the noise of the data
- The effects of using a Fourier transform on the ultrasound images prior to performing a DIC analysis should be studied
- High-strain images were not successfully analyzed when an ROI with only one region was used

Bibliography

Biscaia, Hugo, et al. “Stainless Steel Bonded to Concrete: An Experimental Assessment Using the DIC Technique.” *International Journal of Concrete Structures and Materials*, vol. 12, no. 1, 30 Jan. 2018, pp. 137–156., doi:10.1186/s40069-018-0229-8.

Blaber, Justin, and Antonia Antoniou. “Ncorr Instruction Manual Version 1.2.2.” *Ncorr*, 13 June 2017, www.ncorr.com/download/ncorrmanual_v1_2_2.pdf.

Blaber, J., et al. “Ncorr: Open-Source 2D Digital Image Correlation Matlab Software.” *Experimental Mechanics*, vol. 55, no. 6, 31 Mar. 2015, pp. 1105–1122., doi:10.1007/s11340- 015-0009-1.

Chen, Daoyun, et al. “Crack Growth Analysis in Welded and Non-Welded T-Joints Based on Lock-in Digital Image Correlation and Thermoelastic Stress Analysis.” *International Journal of Fatigue*, vol. 110, May 2018, pp. 172–185., doi:10.1016/j.ijfatigue.2018.01.020.

Feng, Y., et al. “Relative Brain Displacement and Deformation during Constrained Mild Frontal Head Impact.” *Journal of The Royal Society Interface*, vol. 7, no. 53, 2010, pp. 1677–1688., doi:10.1098/rsif.2010.0210.

Genovese, Katia, and Donato Sorgente. “A Morphing-Based Scheme for Large Deformation Analysis with Stereo-DIC.” *Optics and Lasers in Engineering*, vol. 104, May 2018, pp. 159– 172., doi:10.1016/j.optlaseng.2017.06.020.

Hardy, Warren N., et al. “A Study of the Response of the Human Cadaver Head to Impact.” *SAE Technical Paper Series*, 2007, doi:10.4271/2007-22-0002.

Kremkau, F W, and K J Taylor. “Artifacts in Ultrasound Imaging.” *Journal of Ultrasound in Medicine*, vol. 5, no. 4, 1986, pp. 227–237. *Web of Science*, doi:10.7863/jum.1986.5.4.227.

Mallory, A. (2010). "Head Injury and Aging: The Importance of Bleeding Injuries." Annals of Advances in Automotive Medicine 54: 51-60.

Niu, Yuling, et al. “An Accurate Experimental Determination of Effective Strain for Heterogeneous Electronic Packages With Digital Image Correlation Method.” *IEEE Transactions on Components, Packaging and Manufacturing Technology*, vol. 8, no. 4, Apr. 2018, pp. 678–688., doi:10.1109/tcpmt.2018.2794505.

Rangel-Castillo, Leonardo, et al. “Management of Intracranial Hypertension.” *Neurologic Clinics*, vol. 26, no. 2, 2008, pp. 521–541., doi:10.1016/j.ncl.2008.02.003.

Rashid, Badar, et al. “Mechanical Characterization of Brain Tissue in Simple Shear at Dynamic Strain Rates.” *Journal of the Mechanical Behavior of Biomedical Materials*, vol. 28, 2013, pp. 71–85., doi:10.1016/j.jmbbm.2013.07.017.

Pan, Bing, et al. “Two-Dimensional Digital Image Correlation for in-Plane Displacement and Strain Measurement: a Review.” *Measurement Science and Technology*, vol. 20, no. 6, 2009, pp. 1–17. *Web of Science*, doi:10.1088/0957-0233/20/6/062001.